Geoscience Frontiers 11 (2020) 2103–2125

HOSTED BY

Contents lists available at ScienceDirect

Geoscience Frontiers

journal homepage: www.elsevier.com/locate/gsf

Multi-stage rodingitization of ophiolitic bodies from Northern Apennines (Italy): Constraints from petrography, geochemistry and thermodynamic modelling

Emma Salvioli-Mariani [a,*], Tiziano Boschetti [a], Lorenzo Toscani [a], Alessandra Montanini [a], Jasmine Rita Petriglieri [a,b,c], Danilo Bersani [d]

[a] Department of Chemistry, Life Sciences and Environmental Sustainability, University of Parma, Parco Area delle Scienze 157/A, 43124, Parma, Italy
[b] Department of Chemistry, University of Torino, Via Pietro Giuria, 10125, Torino, Italy
[c] Institute of Exact and Applied Sciences, Université de la Nouvelle Calédonie, Campus de Nouville, BP R4 - 98851 Nouméa Cedex, New Caledonia, France
[d] Department of Mathematical, Physical and Computer Sciences, University of Parma, Parco Area delle Scienze 7/A, 43124, Parma, Italy

ARTICLE INFO

Handling Editor: Sohini Ganguly

Keywords:
Rodingite
Hydrothermal alteration
Raman spectroscopy
Thermodynamic modelling
Ligurian ophiolite
Northern Apennines

ABSTRACT

The investigated mantle bodies from the External Ligurians (Groppo di Gorro and Mt. Rocchetta) show evidences of a complex evolution determined by an early high temperature metasomatism, due to percolating melts of asthenospheric origin, and a later metasomatism at relatively high temperature by hydrothermal fluids, with formation of rodingites. At Groppo di Gorro, the serpentinization and chloritization processes obliterated totally the pyroxenite protolith, whereas at Mt. Rocchetta relics of peridotite and pyroxenite protoliths were preserved from serpentinization. The rodingite parageneses consist of diopside + vesuvianite + garnet + calcite + chlorite at Groppo di Gorro and garnet + diopside + serpentine ± vesuvianite ± prehnite ± chlorite ± pumpellyite at Mt. Rocchetta. Fluid inclusion measurements show that rodingitization occurred at relatively high temperatures (264–334 °C at 500 bar and 300–380 °C at 1 kbar). Garnet, the first phase of rodingite to form, consists of abundant hydrogarnet component at Groppo di Gorro, whereas it is mainly composed of grossular and andradite at Mt. Rocchetta. The last stage of rodingitization is characterized by the vesuvianite formation. Hydrogarnet nucleation requires high Ca and low silica fluids, whereas the formation of vesuvianite does not need CO_2-poor fluids. The formation of calcite at Groppo di Gorro points to mildly oxidizing conditions compatible with hydrothermal fluids; the presence of andradite associated with serpentine and magnetite at Mt. Rocchetta suggests Fe^{3+}-bearing fluids with fO_2 slightly higher than iron-magnetite buffer. We propose that the formation of the studied rodingite could be related to different pulses of hydrothermal fluids mainly occurring in an ocean-continent transitional setting and, locally, in an accretionary prism associated with intra-oceanic subduction.

1. Introduction

Rodingites are Ca-rich, Si-undersaturated and alkali-poor rocks of metasomatic origin. The mineral association dominated by Ca–Al and Ca–Mg silicates such as vesuvianite, diopside, grossular, hydrogrossular, andradite and prehnite mirrors these chemical features. Relics of clinopyroxene, olivine and plagioclase can be preserved in Fe- and Mg-rich and alkali-poor protoliths (gabbros and basalts; Hatzipanagiotou et al., 2003). Regardless of the initial composition of the protolith, an advanced rodingite transformation leads to the crystallization of large amounts of diopside, garnet and chlorite.

The rodingites are invariably associated with serpentinites, as lenses or boudins in serpentine cataclasites or as metasomatic alteration zones at the contact between serpentinites and basic rocks. They occur in different geodynamic setting including present-day seafloor, Archean greenstone belts and fore-arc crust (Dal Piaz, 1969; Honnorez and Kirst, 1975; Dal Piaz et al., 1980; Schandl et al., 1989; Dubińska, 1995; O'Hanley, 1996; Hatzipanagiotou et al., 2003). Rodingitization events associated to meta-ophiolites have been also found in Western Alps (Ferrando et al., 2010 and references therein). Microthermometric data on fluid inclusions in diopside, garnet and epidote of rodingites from several localities suggest that serpentinization and rodingite formation

* Corresponding author.
E-mail address: emma.salviolimariani@unipr.it (E. Salvioli-Mariani).
Peer-review under responsibility of China University of Geosciences (Beijing).

https://doi.org/10.1016/j.gsf.2020.04.017
Received 17 May 2019; Received in revised form 14 February 2020; Accepted 12 April 2020
Available online 21 May 2020

mainly occur at shallow conditions ($P < 1$ kbar) and temperature lower than 500 °C (O'Hanley, 1996). However, more recently pressures up to 10 kbar have been inferred (Li et al., 2007). Schandl et al. (1989) identified several conditions of rodingitization and subdivided the rodingites into three groups characterized by increasing metamorphic grade, i.e. epidote-rich (with minor amounts of diopside and titanite), grossular-rich (hydrogrossular, prehnite, with minor amounts of diopside) and diopside-rich rodingites.

The formation of rodingites and the features of the metasomatic fluids are widely discussed. The common association of rodingites with serpentinites and their absence in fresh peridotites support that rodingitization and serpentinization processes are closely related (Coleman, 1977; O'Hanley et al., 1992; Dubińska, 1997; Schandl and Mittwede, 2001; Hatzipanagiotou et al., 2003; Frost et al., 2008). The Ca released by pyroxene alteration during serpentinization is not sufficient to form the observed assemblages dominated by Ca-silicates. In fact, many studies have shown that it is necessary to invoke the presence of Ca-rich hydrothermal fluids (possibly seawater-related, as supported by stable isotope data, see Rösli et al., 1991) and/or fluids leaching the associated basic rocks (De, 1972; Hall and Ahmed, 1984; Hatzipanagiotou and Tsikouras, 2001). On the other hand, Frost et al. (2008) argued that the silica activity play a major role in the formation of rodingitic assemblages, proposing that they may locally originate by silica loss more than by Ca addition. In any case, rodingite is the result of a multistage process where the final chemistry depends on the chemistry of the protolith, the composition and properties of the fluid phase and the physico-chemical conditions during metasomatism.

Our work is focussed on different types of rodingitic assemblages found in the External Ligurian ophiolites from the Northern Apennines (Northern Italy). We present new mineralogical, geochemical and fluid inclusion data, in order to provide petrological constraints on the origin of the investigated mineral associations. Particular attention has been paid to the fluid/rock reactions, in order to fingerprint the geochemical and physical characteristics of the hydrothermal fluids involved. Thermodynamic modelling of the inferred reactions has been carried out and implications for the geochemical models of metasomatism in ultramafic systems in oceanic crust are discussed.

2. Geological and petrological framework

The ophiolitic sequences from the Northern Apennines are remnants of oceanic and transitional lithosphere of the Ligurian Tethys, which was located between the European and the Adriatic plates. Continental breakup and oceanization occurred in the Lower-Middle Jurassic (Bill et al., 2001; Tribuzio et al., 2016). In the Northern Apennines, the ophiolites occur in two distinct structural units, i.e. Internal (IL) and External (EL) Ligurian Units, which were related to different paleogeographic domains. The ophiolites of the Internal Ligurian Units preserve their primary stratigraphic relations and form the basement of a Late Jurassic–Early Cretaceous sedimentary sequence. An ultramafic serpentinized basement that is discontinuously intruded by gabbroic plutons and covered by pillow lavas, sedimentary breccias or pelagic sediments (e.g. Abbate et al., 1980; Cortesogno et al., 1994; Sanfilippo and Tribuzio, 2011) characterize them. Their lithostratigraphic characteristics reflect an intra-oceanic setting. In particular, these ophiolites record a pre-orogenic, ductile to brittle tectono-metamorphic evolution (Cortesogno et al., 1994; Molli, 1996; Tribuzio et al., 2014) and are considered as on-land analogues of oceanic lithosphere originated at slow-spreading centres (Barrett and Spooner, 1977; Tribuzio et al., 2004, 2014). Rodingitic assemblages were found in the gabbros along igneous contacts with the mantle rocks (Cortesogno et al., 1994) and in the basaltic and plagiogranite dikes intruding the peridotites (Barriga and Fyfe, 1983; Borsi et al., 1996). The rodingitization process was associated with relatively high-temperature ocean floor metamorphism leading to nearly complete serpentinization of the peridotites (Tribuzio et al., 2016).

The External Ligurian ophiolitic sequences occur as large slide-blocks within sedimentary melange related to the inception of convergence-related sedimentation in Upper Cretaceous times (see Marroni et al., 2001 and references therein). The ophiolites consist of exhumed subcontinental mantle (Rampone et al., 1995; Montanini et al., 2006), MOR-type basalts and rare gabbroic rocks (Montanini et al., 2008) together with continental crust bodies locally displaying primary relationships with the ophiolites (Marroni and Treves, 1998). This association has been interpreted as embryonic oceanic lithosphere formed in an ocean-continent setting similar to present-day magma-poor passive margins (Marroni and Treves, 1998; Marroni et al., 2001). The ultramafic bodies have variable size, ranging from only some tenths of metres to a few kilometres. The peridotites are Ti-amphibole-bearing spinel lherzolites with a fertile geochemical signature (Rampone et al., 1995) and widespread spinel or garnet pyroxenite layers (Beccaluva et al., 1984; Montanini et al., 2006, 2012; Borghini et al., 2016). The origin of the pyroxenite layers have been attributed to melting of recycled crustal material (Montanini et al., 2012; Montanini and Tribuzio, 2015) or of hybrid eclogite-bearing peridotites (Borghini et al., 2013, 2016) followed by melt/peridotite reactions.

The External Ligurian mantle bodies represent subcontinental lithosphere exhumed to the ocean floor in response to Mesozoic lithospheric thinning and opening of the Jurassic Ligurian-Tethys (Montanini et al., 2006). Evidence for an early stage of equilibration at deep lithospheric levels (T ~1100 °C, P ~2.8 GPa) was recorded by some garnet-bearing pyroxenites. In the peridotites, the subsolidus decompression from spinel to plagioclase stability field was locally accomplished by development of plagioclase-facies mylonitic deformation along hectometre-sized shear zones. Several mantle bodies from the External Ligurian ophiolites also record interaction and refertilization by MOR-type melts during rifting and ocean opening, resulting in plagioclase-enriched impregnated peridotites (Piccardo et al., 2004) intruded by MOR-type gabbros and basalts of Jurassic age (Montanini et al., 2008; Tribuzio et al., 2016). The high temperature deformation recorded by plagioclase mylonites was overprinted by a widespread polyphase brittle deformation under decreasing temperature conditions, coupled with hydration. The reconstructed brittle evolution includes an amphibolite-facies stage, followed by low-temperature hydrothermal alteration and serpentinization associated with polyphase cataclasis and veining stages. The formation of rodingite assemblages (including prehnite, grossular and diopside) have been previously reported only for some gabbroic rocks and basaltic dikes intruding the External Ligurian peridotites (Montanini et al., 2008).

3. Field occurrence

The investigated rocks were sampled in ophiolitic sequences from three localities of the Northern Apennines: Mt. Rocchetta, Campeggi quarry and Groppo di Gorro (Fig. 1). All the investigated bodies belong to the Casanova Complex, a sedimentary melange consisting of coarse clastic deposits with interbedded turbidites of Lower Campanian age and slide-blocks of continental and oceanic lithosphere (Naylor, 1982; Elter et al., 1991).

In the Taro valley, several bodies of highly serpentinized peridotites occur over a wide area; the largest outcrop (Groppo di Gorro) extends between the towns of Berceto and Borgotaro (Fig. 1). Here the mantle rocks stretch over 7 km and have a thickness of 150–200 m (Vescovi et al., 2002). Serpentinites have a dark green or purplish colour and vary from massive to intensely fractured. The protoliths are deeply transformed and relics of the primary mantle assemblage are often recognizable only as serpentine pseudomorphs (Vescovi et al., 2002). Green or black pyroxene porphyroclasts and tiny Cr-spinels with whitish rims of altered plagioclase have been preserved in places (Fig. 2a). Serpentinites with cataclastic texture and complex serpentine (±carbonates) veining patterns may occur along the margins of the serpentinite blocks. Centimetre-thick, strongly altered pyroxenite layers with large, irregularly shaped, dark green spinel have been locally found. The samples of

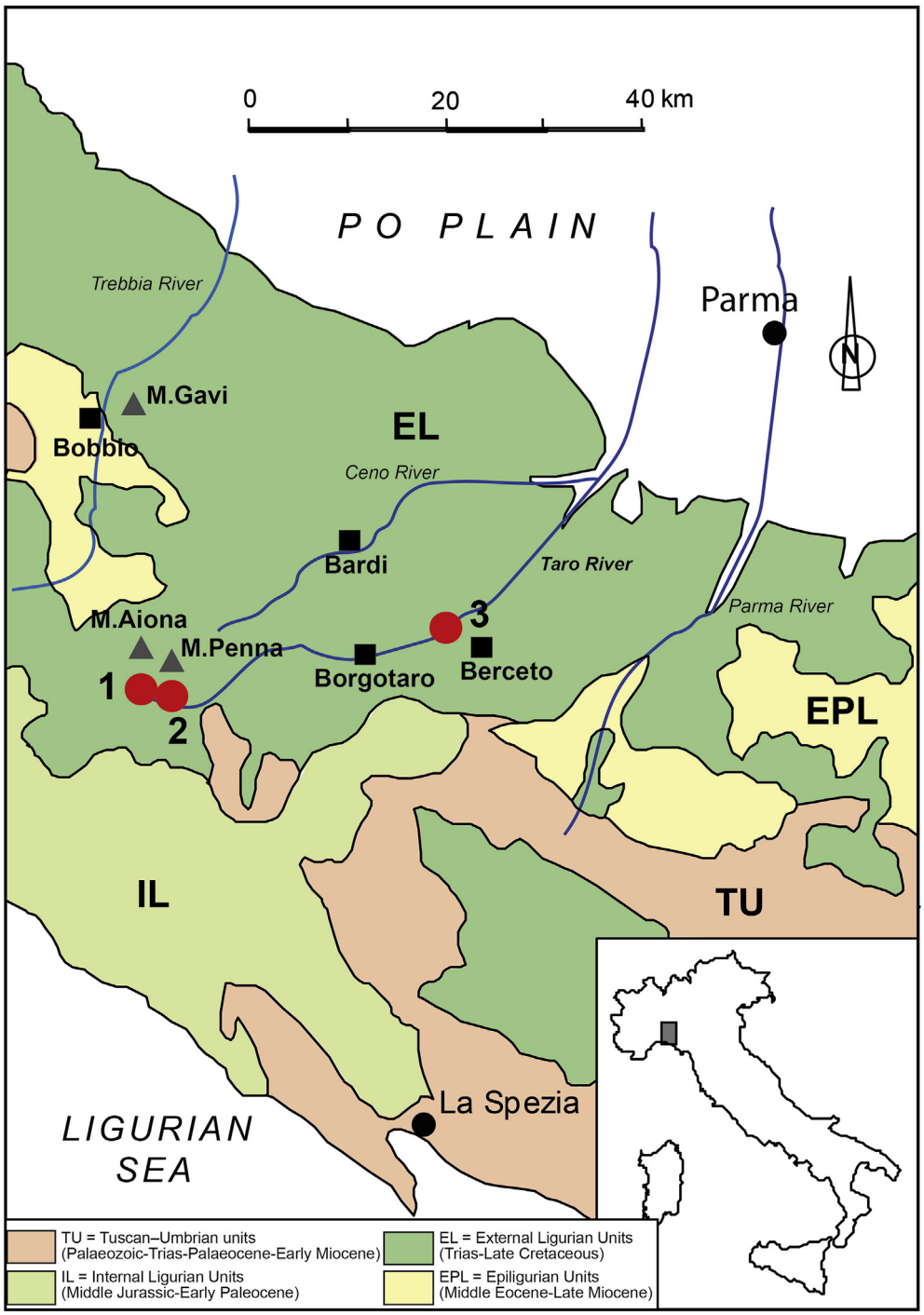

Fig. 1. Tectonic sketch map of the Northern Apennines and main investigated ophiolite outcrops (red circles). 1 = Mt. Rocchetta, 2 = Campeggi quarry, 3 = Groppo di Gorro.

this study have been collected from a quarry located on the northeastern slopes of Groppo di Gorro (GG), on the right side of the Taro river. The rodingites form irregular masses and veins within the serpentinized peridotite and have a lighter colour with respect to the dark green surrounding ultramafic rocks. The size of the rodingite bodies is generally 30–60 cm, rarely up to ~1 m (Adorni, 2001). The rodingite blocks contain relics of spinel-bearing, coarse grained pyroxenites with large pyroxene porphyroclasts (Fig. 2b).

The ultramafic rocks of Mt. Rocchetta and Campeggi (MR) are exposed SW of the Mt. Penna-Mt. Aiona ophiolitic bodies (Fig. 1). The sampling was carried out at two different sites: on the slope of Mt. Rocchetta, at an altitude of 1490 m, and near Campeggi, in a former small quarry and associated debris, at an altitude of 1020 m. The mantle rocks of Mt. Rocchetta are mainly formed by massive peridotites with high degree of serpentinization and local occurrence of metre-sized lenses of relatively fresh peridotites. In places, mafic rocks ranging in composition from olivine-rich gabbro to troctolite intrude the serpentinites (see also Casnedi et al., 1993). The gabbroic intrusives occur both as decimetre-thick lenses showing fuzzy contacts with the host rocks or centimetre-thick dikes. In the nearby Campeggi quarry, the peridotites are relatively fresh spinel-plagioclase lherzolite with coarse-grained porphyroclastic texture and a well-developed foliation. Plagioclase can

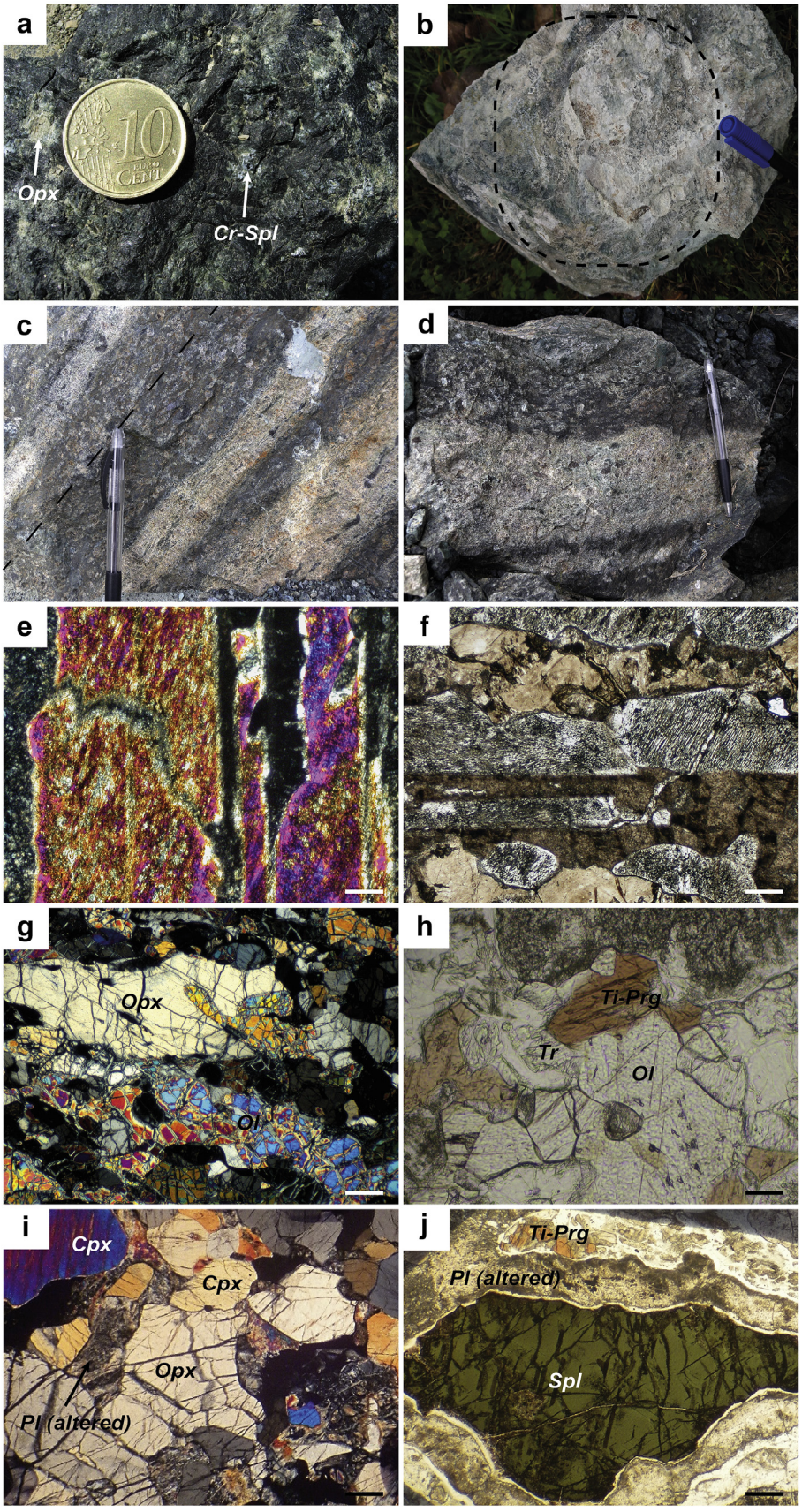

Fig. 2. Field (a–d) and optical microscope (e–j) photographs of the protoliths and their primary parageneses. (a) Groppo di Gorro massive serpentinized peridotite with rare pyroxene prorphyroclast relics (light green) and black Cr-spinel with altered plagioclase rim. (b) Groppo di Gorro rodingite with pyroxenite relics characterized by large pyroxenes and spinel rimmed by whitish plagioclase. (c) and (d) Mt. Rocchetta peridotites with layers of partially rodingitized pyroxenite sub parallel to the peridotite foliation. (e) Altered orthopyroxene lamellae (dark grey) and (f) plagioclase (brown) formed at the expense of clinopyroxene as a result of reaction with percolating melts (sample GG4), Groppo di Gorro. (g) Primary olivine (Ol) + pyroxene (Opx) + spinel (black) in the Mt. Rocchetta peridotite (sample MR3). (h) Ti-pargasite (Ti-Prg) locally replaced by tremolite (Tr) associated with neoblast of olivine (Ol) (peridotite of Mt. Rocchetta, sample MR1). (i) Clinopyroxene with subordinate orthopyroxene and altered plagioclase and (j) green spinel rimmed by altered plagioclase and Ti-pargasite (pyroxenite of Mt. Rocchetta, sample MR10). Dimensional bar 201.6 μm for (g, i, j), and 100.8 μm for (e, f, h).

occur as spinel rims or interstitial patches. These peridotites contain frequent pyroxenite layers concordant with the foliation of the host peridotite and ranging in thickness of 2–15 cm (Fig. 2c and d). The pyroxenites are coarse-grained, clinopyroxene-rich rocks characterized by dark green spinel elongated along the foliation and rimmed by plagioclase. Locally, the pyroxenite abundance can be as high as 20%–30%. Sharp margins between peridotite and pyroxenite are observed. The rodingite mineral assemblage occurs as veins and centimetre-sized patches in peridotite and pyroxenite. They may be highlighted by the presence of whitish or yellowish-green surfaces (with thickness up to a few cm) where small crystals of yellow or yellowish-green (Campeggi quarry) or emerald green garnet (Mt. Rocchetta eastern slope) are clearly visible. As a whole, the rodingite metasomatism seems less pervasive than in the former Groppo di Gorro outcrops.

4. Analytical methods

Whole-rock analyses were performed at Activation Laboratories Ltd., Ancaster, Canada. Eleven samples were selected and analysed for major and trace elements according to Code "4 Litho" package following lithium metaborate/tetraborate fusion. Major oxides were analysed by a combination simultaneous/sequential Thermo Jarrell-Ash ENVIRO II ICP or a VarianVista 735 ICP; calibration is performed using 7 prepared USGS and CANMET certified reference materials (Sparkes, 2017; Actlabs, 2018). Minor/trace elements were analysed by PerkinElmer Sciex ELAN 6000, 6100 or 9000 ICP-MS; three blanks and five controls (three before the sample group and two after) were analysed per group of samples (Sparkes, 2017; Actlabs, 2018). The "4 Litho" package results in a relative standard deviation from replicate analyses of <5% for major elements, and <10% for minor/trace elements, with uncertainties associated with the various determinations being +15% at × 10 detection limit, and +5% at × 100 detection limit (Keighley, 2013; Actlabs, 2018). FeO content was analysed by titration.

The mineral analyses were carried out with a Jeol JSM 6400 Scanning Electron Microscope equipped with a windowless Oxford INCA EDS detector. Operating conditions were 15 kV and 1.2 nA, electron beam about 1 μm in diameter and 100 s counting time; errors are ±2%–5% for major elements and ±5%–10% for minor components while detection limits are ~0.1 wt%. The standards used for calibration are Ni, V, Cr_2O_3, $BaSO_4$, CaF_2, $SrTiO_3$, ilmenite, chromite, glass, olivine, augite, microcline, anorthoclase, apatite.

The micro-Raman measurements were obtained using a Jobin-Yvon Horiba LabRam spectrometer equipped with a He–Ne laser (emission line 632.8 nm) and a doubled Nd:YAG laser (473.1 nm emission line). The spectral resolution ranges between 2 and 3 cm^{-1}, depending on the source. The confocal hole was adjusted in order to obtain a spatial (lateral and depth) resolution of ~2 μm. The spectra were acquired using an ultra-long working distance 50 × and 100 × objectives (N.A. 0.75). The calibration was made using the 520.7 cm^{-1} Raman line of silicon. During the acquisition of the spectra, some emission lines of gas fluorescence lamps were used as standards. The uncertainty on the Raman peak position, obtained by Gauss-Lorentzian deconvolution, is lower than 0.5 cm^{-1}. A wide spectral range (100–3800 cm^{-1}) was scanned for each inclusion. The final acquisitions were made between 100 and 1200 cm^{-1} for the identification of the characteristic vibration of different minerals and between 3300 and 3800 cm^{-1}, the OH-stretching region, for the identification of the serpentine polymorphs and the evaluation of OH contents in garnet. The acquisition time for each spectral window was 120–240 s, with two accumulations. The power on the sample surface is nearly 1 mW. The presence of a motorized support in the X and Y directions with a spatial resolution of about 1 μm and of an autofocus system allowed the realization of two-dimensional and three-dimensional maps.

Micro-thermometric measurements on fluid inclusions were performed using a Linkam THMSG 600 freezing/heating stage equipped with a LNP95 freezing control system and a Lynksys32 system control and image capture software. The stage calibration was carried out with the melting temperature of CO_2, CO_2-clathrate, H_2O, the eutectic temperature of H_2O–NaCl and the critical homogenization temperature of H_2O; the estimated precision of the data is ±0.4 °C. After freezing, the heating rate was maintained at 5 °C/min up to room temperature and then it was increased to 10 °C/min up to about 200 °C and reduced to 2 °C/min until total homogenization.

Thermodynamic reaction path models were calculated to infer the evolution of fluid-rock reactions involved in the rodingite formation. A two-step speciation, the use of implemented thermodynamic databases and different codes were necessary for the speciation/saturation index calculation and construction of the activity diagrams (Boschetti et al., 2016). In the first step, physico-chemical composition of Na–Ca–Cl (Palandri and Reed, 2004) and Ca–OH (Boschetti et al., 2013a, 2013b; Boschetti and Toscani, 2008; Marini and Ottonello, 2002) serpentinizing fluids of seawater and meteoric origin, respectively, were recalculated at 300 °C and 0.5 and 1 kbar by EQ 3/6 software (Wolery and Jarek, 2003). Afterwards, the dissolved species activities and the minerals saturation indexes and volumes resulting from fluid-basalt (diopside 0.6 – anorthite 0.4; Morse, 1980) interaction were plotted by "React" and "Act2" tool, respectively, of The Geochemist's Workbench Workbench® (GWB), version 7.0.6 (Bethke and Yeakel, 2008). In these latter cases, two original thermodynamic databases were constructed at isobaric pressure of 0.5 and 1 kbar and temperature between 50 and 400 °C, respectively (Supplementary Materials). First, preliminary datasets were extracted from the file slop07.dat (http://geopig.asu.edu/sites/default/files/slop07.dat) and converted in the thermo.com.v8.r6.dat format by DBcreate software (Kong et al., 2013). The datasets were then integrated with the thermodynamic data for hydrogrossular (Matschei et al., 2007; Dilnesa et al., 2014), hydrogarnet/katoite, tobermorite and xonotlite (Wolery and Jove-Colon, 2007), lizardite (Wilson, 2010; Holland and Powell, 2011; Blanc et al., 2012) and vesuvianite (Holland and Powell, 2011). According to Bach and Klein (2009), aqueous ion-couples as $NaSO_4^-$, $MgSO_4^0$ (McCollom and Shock, 1997; Blanc et al., 2012) and Al-bearing species (Tagirov and Scott, 2001) were also added to the databases.

5. Results

5.1. Petrography and mineralogy

The mineral associations of all the investigated samples, both rodingite (massive and veins) and preserved peridotite/pyroxenite, are reported in Table 1.

5.1.1. Primary mantle assemblages

The ultramafic rocks of Groppo di Gorro are characterized by widespread hydrothermal alteration. The peridotites show massive, coarse-grained granular textures. Olivine is totally replaced by mesh-texture serpentine that, in turn, is pseudomorphosed by chlorite. Large orthopyroxenes are usually transformed into fibrous grey serpentine (bastite). Relics of the primary mantle assemblage are mainly represented by large fresh clinopyroxenes (up to 10–12 vol%). Spinel is generally altered to opaque Mg-chromite (+chlorite) but small relics of dark brown, "holly-leaf" spinel are observed in places. Plagioclase is almost completely altered to very fine-grained whitish aggregates of grossular-rich garnet. The spinel pyroxenite layers are coarse-grained undeformed rocks with extensive alteration. The original mantle assemblage was most likely composed of clinopyroxene and large green spinel, which were partially replaced by reaction zones containing plagioclase + orthopyroxene (Fig. 2e and f) and olivine + Cr-spinel, respectively. The association diopside, vesuvianite, chlorite occurs as irregular patches along cleavage traces of clinopyroxene, symplectitic intergrowths with orthopyroxene around clinopyroxene and coronas around spinel.

The peridotites from Mt. Rocchetta and Campeggi quarry are foliated spinel-plagioclase lherzolites with coarse-grained porphyroclastic

Table 1
Minerals of the primary mantle assemblage, rodingite (massive and veins) assemblage.

Sample	Relics of the primary mantle assemblage	Protolith	Rodingite assemblage	
			massive	veins
GG1	Cpx, Al-Spl (green)	pyroxenite	Chl1, Chl2, Grt	
GG2	Cpx, Cr-Spl (brown)	pyroxenite	Chl1, Di, Ves, Grt, Chl2, Cc	Chl2 with Grt Chl2 with Grt and Di
GG3	Cpx, Cr-Spl (brown)	pyroxenite	Chl1, Di, Ves, Chl2, Grt, Cc	
GG4	Cpx, Cr-Spl (brown)	pyroxenite	Chl1, Ves, Di, Grt, Chl2, Cc	
GG5	Cpx, Cr-Spl (brown)	pyroxenite	Chl1, Di, Grt, Cc	
MR1	Cpx, green/ brownish green Spl, Ol, Amph	peridotite	Srp1, Grt, Chl, Di, Prh, Pmp, Mt	Srp2, Grt, Srp2 with Di and Mt
MR2	Cpx, Ol, Cr-Spl (brown)	peridotite	Srp1, Mt, Grt	
MR3	Cpx, Ol, Cr-Spl (brown), Opx, Sulfides	peridotite	Srp1, Mt, Grt	
MR4	brownish green Spl	pyroxenite	Srp1, Mt	Di, Srp2, Chl2
MR6	Cpx, Opx, Ol	pyroxenite	Srp1, Di, Grt, Ves, Srp2	Ves in Di
MR10	Cpx, Opx, Spl, Amph	pyroxenite	Srp1, Di	Grt
MR15	Cpx	pyroxenite	Grt, Srp1, Chl2, ±Di, ±Ves	Grt
MR18	Spl	pyroxenite	Srp1, Grt, Chl2	
MR19		breccia	Srp1, Grt	Srp2, fibrous brown Grt
MR21	Spl	peridotite	Srp1, Srp2	Colourless Grt, fibrous brown Grt without and with Srp2, Srp2

Chl, chlorite; Srp, serpentine; Grt, garnet; Di, diopside; Ves, vesuvianite; Prh, prehnite; Pmp, pumpellyite; Mt, magnetite; Cpx, clinopyroxene; Ol, olivine; Opx, ortopyroxene; Amph, amphibole (Ti-pargasite). 1, first generation (mash texture); 2, second generation (rodingite).

textures and clinopyroxene amounts up to 12–15 vol%. Large porphyroclasts of ortho- and clinopyroxene are surrounded by smaller polygonal or irregularly shaped neoblasts of olivine ± pyroxene ± spinel ± brown amphibole (Fig. 2g and h). Mutual pyroxene exsolutions may occur in these porphyroclasts. Olivine shows a partial replacement by mesh-textured serpentine + magnetite and widespread relics occur. Small amounts of disseminated light brown amphibole (Ti-pargasite) are locally replaced by colourless tremolite (Fig. 2h). The spinel is brownish-green to brown, partially or totally replaced by garnet and diopside or surrounded by an association of microcrystalline vesuvianite, chlorite, prehnite, pumpellyite and garnet. Plagioclase, mainly altered to prehnite, occurs as rim around brown spinel grains. In the altered peridotite, serpentine shows the typical mesh texture. Serpentine often occurs as veins (millimetric to centimetric in size) with fibrous texture or as silky patinas.

Pyroxenite layers, similar to those described by Borghini et al. (2016) in the Suvero massif, are websterites with dominant clinopyroxene, subordinate orthopyroxene and large green spinel rimmed by altered plagioclase; trace amounts of ilmenite and Ti-amphibole may be present (Fig. 2i and j).

Textural observations and mineralogy suggest different protoliths for the rodingites from Groppo di Gorro and Mt. Rocchetta. The inference of the possible protoliths is mainly based on the observed relict assemblages and/or on textural and mineralogical similarities with fresh samples from the same outcrop or from similar ophiolitic bodies. In particular, the rodingites from Groppo di Gorro contain spinel pyroxenite relics (Fig. 2b) resembling the fresh spinel pyroxenites from the Mt. Gavi mantle body (Montanini et al., 2017 and unpublished data), whereas the rodingites from Mt. Rocchetta contain abundant peridotite (olivine + orthopyroxene + clinopyroxene + spinel) remnants and are associated with spinel pyroxenite. The close association of peridotite and spinel-bearing pyroxenite found at Campeggi (samples CAM2 and CAM8) further supports their inference as protoliths for the Mt. Rocchetta rodingite.

5.1.2. Rodingite assemblage

The rodingite bodies and veins at Groppo di Gorro (hereafter GG) consist of the association diopside + vesuvianite + garnet + calcite + chlorite (Fig. 3a–c). At Mt. Rocchetta-Campeggi (hereafter MR), the rodingite metasomatism was confined to veins and volumetrically limited impregnations (Fig. 3d–f), yielding an association of garnet + diopside + serpentine ± prehnite ± pumpellyite ± vesuvianite ± chlorite.

Garnet is widespread in the rodingite zones, where it occurs with different features. (i) Brownish microcrystalline aggregates with cloudy appearance crystallize around or within the oxides (often associated with altered plagioclase) or along the cleavages of altered primary pyroxene (Fig. 3g). Rare aggregates of dark brown-green or emerald green garnet occur around Cr-rich spinel relics at GG (Fig. 3h), whereas garnet in association with prehnite, pumpellyite, chlorite and serpentine derives from the transformation of oxides and/or olivine at MR. (ii) Idiomorphic to sub-idiomorphic small garnet crystals with a birefringent rim occur in association with vesuvianite and diopside; locally, they are included in calcite at GG (Fig. 3i) or in fresh clinopyroxene at MR (Fig. 3j). (iii) Idiomorphic garnet with birefringent rim is associated with diopside in chlorite veins at GG (Fig. 3k). (iv) Veins of colourless and birefringent sub-idiomorphic garnet and of brownish and fibrous garnet occur in totally serpentinized areas at MR (Fig. 3l). (v) Large birefringent idiomorphic garnet shows oscillatory zoning with six-sector twinning at MR (Fig. 3m); locally, garnet is partially overgrown by serpentine. (vi) Small garnet crystals with irregular margins and cloudy core may contain magnetite (Fig. 3n).

Colourless *diopside* occurs as: (i) small prismatic crystals in association with garnet in altered plagioclase, along the boundaries of altered clinopyroxene and olivine and in their cleavages and fractures; (ii) crystals associated with garnet, vesuvianite and chlorite to form the rodingite association (Fig. 3a, b, d, f, j); (iii) elongated prismatic crystals in veins of serpentine at MR (Fig. 3o) and in veins of chlorite + garnet at GG (Fig. 3k).

Vesuvianite occurs as prismatic crystals with pyramidal termination locally arranged to form fibrous-radial aggregates (Fig. 3a–d, f, j) associated with garnet, diopside and chlorite. Vesuvianite crystals from GG are larger and more abundant than at MR and the basal section of the prismatic crystals shows a central portion with a cribrous appearance. At MR, vesuvianite sometimes occurs as small vein crosscutting diopside (Fig. 3f).

Chlorite is widespread at GG where it shows a mesh-texture suggesting a pseudomorphic substitution of serpentine (Chl1). Chlorite at GG also occurs as (i) veins of colourless needle-like crystals (Chl2) grown perpendicularly to the walls of the fractures and associated with garnet and diopside (Fig. 3k), (ii) brownish fibers and (iii) small rounded clumps. Locally, overgrowth of chlorite laths on diopside and garnet are observed (Chl2, Fig. 3a). Chlorite is rare at MR where it is associated with garnet, vesuvianite, prehnite and pumpellyite in the alteration zone around the oxides (Chl2). It also occurs as small laths with a bright green colour or in colourless radially arranged needle-like crystals on the edges of serpentine and diopside veins (Chl2, Fig. 3o).

Serpentine occurs only in the MR samples, whereas at GG it is replaced by pseudomorphic chlorite. The presence of serpentine, resembling

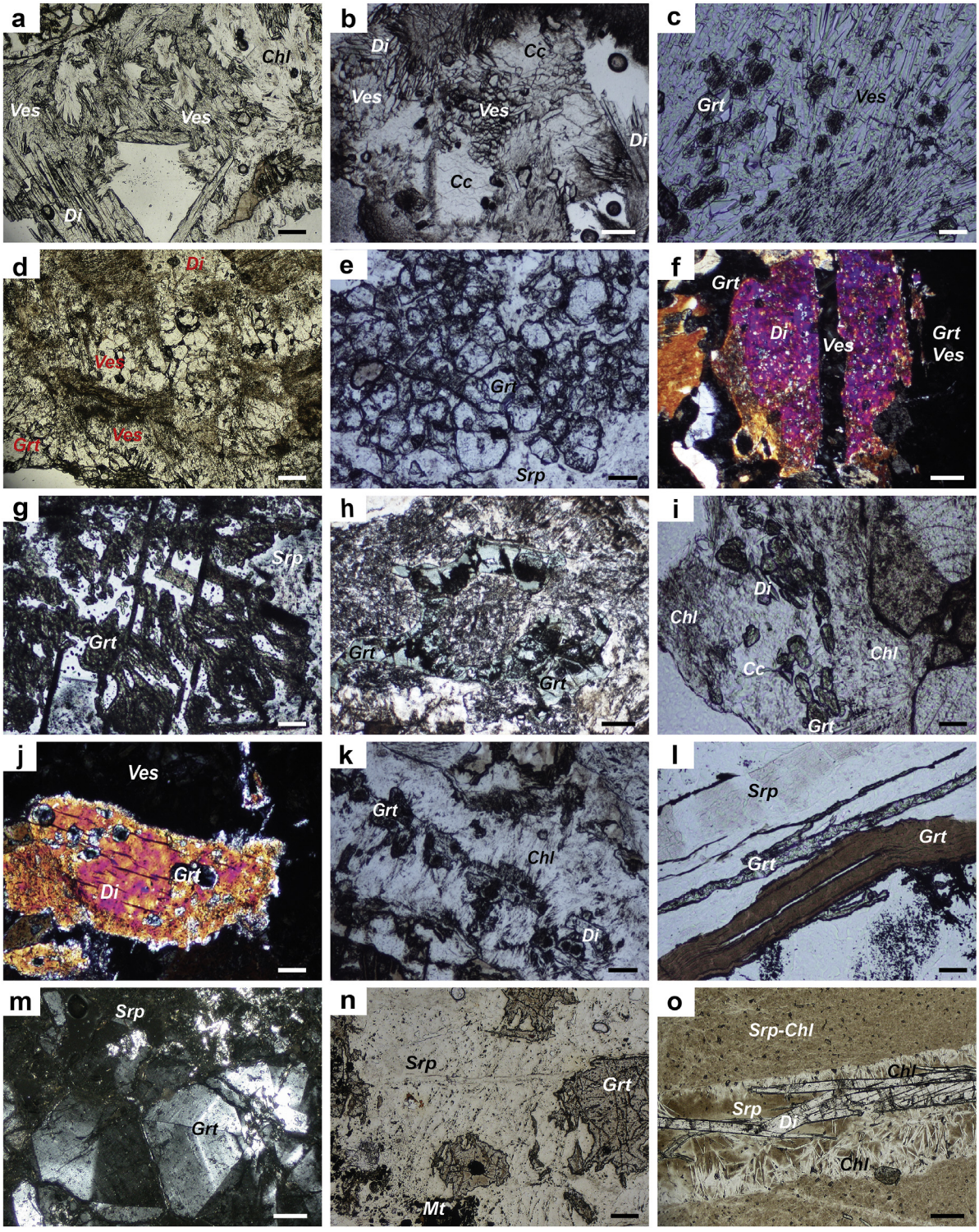

Fig. 3. Optical microscope photographs showing the paragenetic assemblage of the rodingites from Groppo di Gorro (GG) and Mt. Rocchetta (MR) and the different types of garnet. (a) Association of chlorite (Chl), diopside (Di) and vesuvianite (Ves) (sample GG4). (b) Association of calcite (Cc), vesuvianite and diopside (sample GG2). (c) Garnet (Grt) with birefringent rim associated with vesuvianite (sample GG3). (d) Vesuvianite and diopside (sample MR15). (e) Garnet in serpentine (Srp) (sample MR6). (f) Vesuvianite associated with garnet and diopside as vein crossing diopside (sample MR6). (g) Type (i) microcrystalline aggregates of brownish garnet with cloudy appearance along the cleavage traces of partially or totally transformed pyroxene (sample GG1) and (h) aggregates of emerald green garnet around pre-existing oxides (sample GG2). (i) Type (ii) idiomorphic to sub-idiomorphic small crystals of garnet in calcite (sample GG1) and (j) idiomorphic small crystals of garnet in diopside (sample MR6). (k) Type (iii) idiomorphic crystals of garnet with birefringent rim associated with diopside in the middle of chlorite vein (sample GG2). (l) Vein filled by type (iv) colourless and brownish garnet in a serpentinized portion (sample MR21). (m) Type (v) large birefringent crystals of idiomorphic garnet in serpentine showing oscillatory zoning and six-sector twinning radiating from the center of the crystal (sample MR15). (n) Type (vi) small rounded crystals of garnet showing extremely irregular shape with a cloudy core sometimes containing magnetite (sample MR21). (o) Vein of serpentine containing diopside surrounded by chlorite (sample MR4). Dimensional bar 50 μm for (a, c, d, g, i, j, l, n), 201.6 μm for (b, f, h, m, o), and 100.8 μm for (e, k).

lizardite, is evidenced by the mesh-texture on olivine, pseudomorphic substitution of pyroxene with alignments of garnet along the cleavage traces (Fig. 3g) and by colourless rims around spinel (Srp1). The serpentine portions are crossed by veins of fibrous type (iv)-garnet (Fig. 3l); areas with small amount of radiating fibres of serpentine contain idiomorphic, twinned and zoned type (v)-garnet (Fig. 3m). Overgrowths of serpentine (Srp2) on garnet (Fig. 3n) and pseudomorphic substitution of garnet locally occur. The mm-to cm-sized veins of serpentine (Srp2) are abundant; veins are deformed and cross each other supporting a polyphase generation. Serpentine of the veins is fibrous and can be associated with radially arranged needle-like chlorite, prismatic diopside (Fig. 3o) and/or idiomorphic magnetite.

Cubic *magnetite* is abundant in the serpentine veins and in the serpentinized areas of MR samples. Magnetite also occurs as rim of relic spinel and of Ni–Fe(-Co)-bearing sulphides (Co-pentlandite) and, rarely, in type (vi)-garnet (Fig. 3n). Needle-like *ilmenite* is associated with magnetite in serpentine.

Prehnite and *pumpellyite* in association with garnet, chlorite, serpentine and vesuvianite occur sometimes around the oxides of MR.

At GG, *calcite* is associated with vesuvianite, diopside and garnet (Fig. 3b, i).

5.2. Mineral chemistry

5.2.1. Primary mantle assemblage

Spinel (Table 2J and Supplementary Material S1). At GG, Cr-rich spinel is compositionally homogeneous (Chr 55%–68%, Cr# 77–89, Mg# 3–11), whereas at MR spinel shows large substitution Al–Cr–Fe^{3+} and Mg–Mn–Fe^{2+}(-Zn) and variable compositions (Sp 46%–74%, Cr# 1–99, Mg# 1–71) (Fig. 4a).

Pyroxenes and *olivine* (Table 2K, L, M and Supplementary Material S1). Primary clinopyroxene has similar composition in both localities being characterized by Mg# 83–89 (GG) and 84–89 (MR), Cr_2O_3 up to 0.86 wt.% and relatively high TiO_2 and Al_2O_3 contents. Orthopyroxene has slightly higher values of Mg# (88–90) and lower contents of Cr_2O_3 than clinopyroxene (up to 0.46 wt.%). Fresh olivine occurs only at MR and shows Mg# in the range 88–90 and NiO contents up to 0.45 wt.%.

The rare *plagioclase* preserved at MR has a bytownite composition ($An_{75}Ab_{25}$, Table 2N and Supplementary Material S1) with small content of iron (FeO^t 0.18 wt.%).

Amphibole (Table 2O and Supplementary Material S1) occurs as rare reddish-brown Ti-pargasite, locally replaced by colourless tremolite (Hawthorne et al., 2012) at MR (sample MR1 and MR10). Ti-pargasite shows quite high content of Cr_2O_3 (up to 1.03 wt.%).

5.2.2. Rodingite assemblage

Garnet (Table 2A and Supplementary Material S1) shows a large compositional variability, particularly for Al, Fe^{3+} and Ti, and mainly contains molecules of grossular, andradite and hydrogarnet (Fig. 4b). The end-member proportions have been calculated following the procedures of Rickwood (1968) after the determination of the hydrogen content and the distribution of Fe^{3+} and Fe^{2+} (cf. Barriga and Fyfe, 1983). The water contents are in the range 0–5.79 wt.% at GG and 0–4.26 wt.% at MR.

The garnet of MR samples is a solid solution of grossular and andradite end-members, but almost pure grossular and andradite have been locally detected; garnet from GG contains high quantity of hydrogarnet and has a more variable composition (Fig. 4b) depending on the primary transformed mineral (clinopyroxene or plagioclase or spinel). MR garnets have the highest Fe_2O_3 and TiO_2 contents (up to 32.7 and 39.4 wt.%, respectively), whereas those from GG reach the highest concentrations of Cr_2O_3 (up to 20.7 wt.%) and uvarovite (up to 51 mol%) particularly in the crystals grown around Cr-spinel relics (Supplementary Material S1). Hydrogarnet is common in GG garnets (up to 42 mol%) whereas in the MR garnets it is lower (up to 18 mol%, only in one case 30 mol%) or absent. MgO is low and rarely high enough to form pyrope (up to 16 mol % at GG and 9 mol% at MR). Type (iv) brownish and fibrous garnet of MR has andradite-rich composition (90–95 mol% And) similarly to porous and cloudy type (vi) garnet (up to 97 mol% And). The large idiomorphic and birefringent type (v) garnet, widespread in the MR rodingites, shows an oscillatory zoning due to the variations of Al, Fe^{3+} and Ti contents and an andradite-rich rim (2 mol% in the core up to 44 mol% in the outermost rim, sample MR15) (Table 2A).

Diopside (Table 2B and Supplementary Material S1). Diopside from GG has a homogenous composition (Mg# 96–99) whereas that of MR is more variable (Mg# 89–100).

Vesuvianite. High concentration of FeO^t (up to 9.64 wt.%) have been observed in vesuvianite from GG (Table 2C and Supplementary Material S1). The negative correlation between total Fe and Al suggests the prevalent presence of iron as Fe^{3+}.

Prehnite and *pumpellyite* (Tables 2D and 2E and Supplementary Material S1). The composition of prehnite is close to the ideal formula with small substitution of Ca by Na (Na_2O up to 0.40 wt.%). Pumpellyite is Al-rich (Al_2O_3 up to 33.9 wt.%).

Chlorite (Table 2F and Supplementary Material S1). Chlorite from GG is richer in Mg and Si (pennine, rarely clinochlore) than MR chlorites (clinochlore, rarely ripidolite, picnochlorite, pennine), where Si and Mg are replaced by Al and Fe, respectively (Fig. 4c). The pseudomorphic chlorite on serpentine at GG has the composition of talc-chlorite (Fig. 4c).

Serpentine (Table 2G and Supplementary Material S1). Fe and Mg contents are quite homogeneous; Al shows the highest concentration (0.411–0.623 Al a.p.f.u) in the fibrous serpentine of the veins (Srp2) (Fig. 3o) and the lowest (up to 0.012 Al a.p.f.u.) in serpentine replacing garnet (Srp2) (Fig. 3n). It consists of lizardite polymorph in both cases (see Raman spectroscopy). Small amounts of Cr (Cr_2O_3 up to 2.91 wt.%) and Ni (NiO up to 0.88 wt.%) occur in serpentine replacing clinopyroxene and olivine, respectively.

Oxides (Tables 2H and 2I and Supplementary Material S1). They consist of almost pure magnetite, with small TiO_2, Cr_2O_3, MgO contents (up to 1.60 wt.%, 2.95 wt.%, 1.53 wt.%, respectively). Ilmenite is very rich in Mn (MnO 22.79–23.49 wt.%).

5.3. Raman spectroscopy

Micro-Raman spectroscopy was applied to selected minerals of the rodingite assemblages (serpentine, garnet, vesuvianite) in order to obtain structural characterization and additional chemical informations.

We have analysed the serpentine occurring in mesh texture or in veins with fibrous appearance associated with chlorite, diopside (Fig. 3o) and, locally, magnetite. In the micro-Raman spectra at low frequencies, this serpentine shows the following peaks (Fig. 5a). The frequency 197 cm^{-1} is ascribed to Mg-(O, OH)$_6$ group vibrations, and 235 cm^{-1} to O–H–O vibrations. The frequencies 386 cm^{-1} and 685 cm^{-1} are ascribed to symmetric bending v_5 of the SiO_4 tetrahedra and Si-O_b-Si stretching vibrations, respectively; lastly, a weak peak at 1096 cm^{-1} is related to antisymmetric Si-O_{nb} stretching vibration (Groppo et al., 2006; Petriglieri et al., 2015a). The OH stretching vibrations in the high wavenumber range 3550–3850 cm^{-1} are diagnostic for the recognition of the serpentine polymorphs (Lemaire et al., 1999; Auzende et al., 2004; Petriglieri et al., 2015b; Petriglieri, 2017). In our samples, serpentine shows the doublet at 3676 and 3702 cm^{-1} (Fig. 5b) which is characteristic of the polymorph lizardite as also supported by the peaks found at low frequencies (Fig. 5a). Sometimes, in addition to the peaks of lizardite, we found other low frequency peaks at 197, 355, 469 and 543 cm^{-1} (Fig. 5a, arrows) characteristic of the main Si–O vibrations of chlorites (Prieto et al., 1991; Kleppe et al., 2003; Wang et al., 2015). In the spectral zone of the OH stretching, the presence of chlorite increases the peak height at 3702 cm^{-1} (Fig. 5b).

In addition, micro-Raman spectroscopy was useful for determining the hydration degree of garnet. In particular, grossular- and andradite-rich garnets show the most significant spectra. The MR garnets show the triplet of the Si–O stretching modes in the 800–900 cm^{-1} spectral range, which is typical of andradite (Fig. 5c) (Bersani et al., 2009). The

Table 2
Representative analyses of minerals from rodingite assemblage (garnet, diopside, vesuvianite, prehnite, pumpellyite, oxides, ilmenite, chlorite, serpentine) and from the primary mantle assemblage (pyroxene, olivine, plagioclase, amphibole, spinel) at Groppo di Gorro (GG) and Mt. Rocchetta (MR).

	(A) Garnet																			
	Type (i)						Type (ii)		Type (iii)		Type (i)			Type (ii)	Type (iv)		Type (v)			Type (vi)
	GG1			GG2	GG4	GG5	GG2*	GG3	GG2		MR1		MR6	MR6	MR10	MR21	MR15			MR21
																	core	ext rim	int rim	
wt.%																				
SiO_2	38.03	31.51	33.31	26.21	36.65	31.71	38.43	36.61	38.52	36.63	36.82	33.54	33.31	40.39	35.94	34.59	38.60	36.36	35.98	34.94
TiO_2	–	0.40	5.27	0.53	0.13	–	0.17	0.11	–	–	–	0.13	26.12	0.26	–	–	1.69	0.59	6.11	0.15
Al_2O_3	15.76	6.31	9.47	9.10	23.52	22.55	14.36	12.00	12.41	23.15	21.34	14.54	6.43	10.40	1.46	–	20.24	11.53	11.75	0.54
FeO^t	9.25	20.14	12.19	3.46	0.46	1.26	10.78	13.61	13.42	0.41	2.89	12.37	1.60	13.12	26.50	28.46	0.73	13.57	9.05	27.76
MnO	–	0.26	–	0.21	–	–	0.20	0.14	–	0.15	0.21	0.23	–	–	0.23	0.12	–	–	–	–
MgO	–	0.27	1.40	0.82	–	0.10	–	5.16	–	–	–	0.16	–	1.47	–	0.21	–	0.14	0.10	0.54
CaO	36.42	35.48	36.48	39.36	37.45	39.31	35.11	31.04	35.26	37.71	36.79	36.21	31.30	33.60	33.78	33.69	36.94	36.01	36.52	33.48
Cr_2O_3	–	–	0.85	14.84	–	0.15	–	–	–	–	–	–	1.03	–	–	–	0.87	0.77	0.33	–
H_2O^1	0.41	2.62	1.42	5.79	1.59	3.49	0.00	1.53	0.00	1.42	1.18	2.26	0.00	0.00	0.17	0.78	0.00	0.72	0.00	0.65
Total	*99.88*	*96.98*	*100.39*	*100.32*	*99.80*	*98.58*	*99.04*	*100.20*	*99.60*	*99.47*	*99.23*	*99.44*	*99.79*	*99.24*	*98.09*	*97.84*	*99.06*	*99.68*	*99.84*	*98.06*
Structural formula on the basis of 24 O																				
Si	5.989	5.416	5.351	4.006	5.405	4.694	6.174	5.733	6.237	5.446	5.575	5.308	5.211	6.518	6.453	6.277	5.910	5.901	5.789	6.297
Ti	–	0.052	0.637	0.060	0.014	–	0.021	0.013	–	–	–	0.016	3.073	0.032	–	–	0.194	0.073	0.739	0.020
Al	2.926	1.278	1.793	1.639	4.088	3.934	2.719	2.215	2.368	4.057	3.808	2.712	1.186	1.978	0.310	–	3.653	2.205	2.228	0.116
Fe^{3+}	1.190	2.895	1.638	0.443	0.000	0.156	1.378	1.783	1.751	0.000	0.259	1.511	0.210	1.771	3.979	4.319	0.093	1.842	1.218	4.184
Fe^{2+}	0.028	0.000	0.000	0.000	0.057	0.000	0.070	0.000	0.066	0.051	0.107	0.125	0.000	0.000	0.000	0.000	0.000	0.000	0.000	0.000
Mn	–	0.038	–	0.027	–	–	0.027	0.018	–	0.019	0.026	0.031	–	–	0.035	0.018	–	–	–	–
Mg	–	0.068	0.334	0.187	–	0.022	–	1.203	–	–	–	0.038	–	0.354	–	0.057	–	0.033	0.023	0.144
Ca	6.146	6.534	6.281	6.445	5.917	6.235	6.043	5.208	6.118	6.008	5.968	6.141	5.247	5.809	6.499	6.551	6.060	6.262	6.297	6.465
Cr	–	–	0.108	1.792	–	0.017	–	–	–	–	–	–	0.127	–	–	–	0.105	0.098	0.042	–
H4	0.185	1.172	0.636	2.593	0.713	1.564	0.000	0.684	0.000	0.638	0.526	1.012	0.000	0.000	0.074	0.348	0.000	0.321	0.000	0.292
	16.464	17.454	16.779	17.192	16.194	16.623	16.432	16.857	16.540	16.219	16.271	16.895	15.053	16.461	17.349	17.570	16.014	16.735	16.337	8.574
Uvr	0.0	0.0	3.0	44.0	0.0	0.4	0.1	0.0	0.2	0.0	0.0	0.0	8.3	0.0	0.0	0.0	2.7	2.4	1.2	0.0
And	28.9	69.4	46.3	12.0	0.0	3.8	33.6	44.6	42.4	0.0	6.4	35.7	13.8	47.2	92.8	93.9	2.4	44.4	34.9	94.0
Pyr	0.0	1.1	6.3	1.5	0.0	0.4	0.2	20.1	0.1	0.0	0.0	0.6	0.0	6.3	0.0	0.0	0.0	0.5	0.4	2.0
Sps	0.0	0.6	0.2	0.0	0.0	0.1	0.4	0.3	0.0	0.3	0.4	0.5	0.3	0.0	0.6	0.0	0.0	0.0	0.0	0.0
Hgr	3.0	18.7	12.0	42.3	11.9	25.4	0.0	11.4	0.0	10.5	8.6	15.9	0.0	0.0	1.1	5.1	0.0	5.2	0.0	4.0
Grs	67.6	10.2	32.2	0.2	87.1	69.9	64.6	23.6	56.2	88.4	82.8	45.1	77.6	46.5	5.5	1.0	94.8	47.5	63.4	0.0
Alm	0.5	0.0	0.0	0.0	0.9	0.0	1.1	0.0	1.1	0.8	1.7	2.0	0.0	0.0	0.0	0.0	0.0	0.0	0.0	0.0
Sch	0.0	0.0	0.0	0.0	0.0	0.0	0.0	0.0	0.0	0.0	0.0	0.2	0.0	0.0	0.0	0.0	0.0	0.0	0.0	0.0

	(B) Diopside		(C) Vesuvianite			(D) Prh	(E) Pmp	(F) Chlorite						(G) Serpentine				(H) Oxides			(I) Ilm
	GG1	MR4	GG2	GG3	MR6	MR1	MR1	GG1	GG3	GG5	MR3	MR15	MR18	MR4	MR21			MR1		MR3	MR3
wt.%																					
SiO_2	55.20	55.47	36.41	37.12	37.06	44.28	34.00	34.69	34.46	31.07	39.09	28.52	26.96	39.73	43.95	44.83	SiO2	0.28	1.45	0.36	1.80
TiO_2	–	–	–	0.21	0.81	–	–	0.14	–	–	–	–	–	0.14	–	–	TiO2	0.55	0.17	–	49.80
Al_2O_3	–	–	17.10	15.03	17.45	25.94	30.78	16.47	16.00	19.70	9.87	21.44	18.12	5.70	–	–	Al2O3	–	–	0.14	0.26
FeO^t	0.77	0.25	3.67	9.64	3.44	–	0.35	0.94	1.11	7.51	4.62	7.71	28.94	3.79	3.78	5.25	Cr2O3	1.31	1.33	0.31	0.15
MnO	0.40	0.11	–	–	–	–	–	–	0.22	0.36	0.22	–	0.52	–	0.26	–	FeOt	91.37	86.77	94.69	22.48
MgO	18.53	18.54	3.06	–	2.15	–	–	35.30	35.67	27.62	35.59	26.63	13.75	36.34	38.56	36.99	MnO	0.33	0.32	0.21	23.38
CaO	25.88	25.77	35.66	35.41	35.84	27.78	30.90	–	–	0.34	0.15	0.15	0.20	–	0.17	–	MgO	0.15	1.39	0.22	2.11
Na_2O	–	–	–	0.11	–	0.23	0.22	–	–	–	–	–	–	–	–	–	CaO	–	–	–	–
Cr_2O_3	–	–	0.10	–	–			–	–	–	–	0.47	–	–	–	–					
NiO								–	–	–	–	–	–	–	–	–					
Total	*100.78*	*100.13*	*95.99*	*97.52*	*96.74*	*98.23*	*96.25*	*87.54*	*87.46*	*86.59*	*89.54*	*84.91*	*88.48*	*85.70*	*86.73*	*87.08*	*Total*	*93.99*	*91.43*	*95.91*	*99.98*
Structural formula on the basis of 6 O Diopside, 24 (O,OH) Prh, 14 (O,OH) Pmp, 28 O Chlorite, 9 (O,OH) Serpentine, 4 O Oxides, 3 O Ilmenite, 50 cations Vesuvianite																					
Si	1.986	1.999	18.061	18.654	18.201	6.458	3.049	6.383	6.365	5.996	7.153	5.631	5.743	2.428	2.653	2.703	Si	0.014	0.073	0.018	0.045

(*continued on next page*)

Table 2 (*continued*)

	(B) Diopside		(C) Vesuvianite			(D) Prh	(E) Pmp	(F) Chlorite						(G) Serpentine				(H) Oxides			(I) Ilm
	GG1	MR4	GG2	GG3	MR6	MR1	MR1	GG1	GG3	GG5	MR3	MR15	MR18	MR4	MR21			MR1		MR3	MR3
Ti	–	–	–	0.079	0.298	–	–	0.019	–	–	–	–	–	0.006	–	–	Ti	0.021	0.006	–	0.929
Al^{IV}	–	–	0.000	0.000	0.000	1.542	0.000	1.617	1.635	2.004	0.847	2.369	2.257		–	–	Al	–	–	0.008	0.008
Al^{VI}	–	–	9.995	8.904	10.101	2.917	3.253	1.956	1.850	2.476	1.282	2.620	2.294	0.411	–	–	Cr	0.052	0.053	0.012	0.003
Fe^{3+}	0.023	0.002															Fe3+	1.893	1.838	1.954	0.064
Fe^{2+}	0.000	0.005	1.493	3.983	1.402	–	0.026	0.145	0.172	1.212	0.707	1.273	5.156	0.194	0.191	0.264	Fe2+	1.011	0.968	0.998	0.398
Mn	0.012	0.003	0.000	–	–	–	–	–	0.035	0.059	0.033	–	0.094	–	0.013	0.002	Mn	0.014	0.014	0.009	0.491
Mg	0.994	0.996	2.263	–	1.572	–	–	9.681	9.820	7.943	9.707	7.836	4.365	3.310	3.469	3.323	Mg	0.011	0.104	0.016	0.078
Ca	0.998	0.995	18.952	19.064	18.863	4.342	2.969	–	–	0.070	0.030	0.032	0.045	–	0.011	–	Ca	–	–	–	–
Na	–	–	–	0.111	–	0.065	0.038	–	–	–	–	–	–	–	–	–					
Cr	–	–	0.039	–	–			–	–	–	–	0.073	–	–	–	–					
Ni								–	–	–	–	–	–	–	–	–					
	4.013	4.001	50.808	50.794	50.438	15.323	9.334	19.801	19.876	19.761	19.759	19.833	19.955	6.350	6.344	6.290		3.015	3.056	3.013	2.014
Mg#	97.7	99.3																			
Wo	49.5	49.8															Sp	0.2	0.0	0.3	
En	49.3	49.8															Mg-Chr	0.7	2.1	0.5	
Fs	1.1	0.4															Mg-Fer	0.0	6.1	0.4	
																	Hrc	0.0	0.0	0.0	
																	Chr	1.3	0.0	0.0	
																	Usp	2.0	0.5	0.2	
																	Mt	95.9	91.3	98.6	

	(J) Spinel					(K) Clinopyroxene				(L) Orthopx			(M) Olivine		(N) Pl	(O) Amph		
	GG3	MR1		MR3		GG2	MR1	MR3	MR10	MR1	MR3	MR10	MR1	MR3	MR1	MR1	MR1	MR10
																Trm	Ti-Prg	Ti-Prg
wt.%																		
SiO_2	0.27	0.14	0.26	–	SiO_2	51.15	51.37	49.56	51.11	55.00	56.31	53.48	40.28	40.63	47.78	57.85	42.09	43.39
TiO_2	2.82	–	0.11	0.32	TiO_2	0.78	1.10	0.90	0.63	0.22	0.25	0.29	–	–	–	–	3.82	2.82
Al_2O_3	3.74	54.03	64.44	39.96	Al_2O_3	4.62	4.91	5.75	6.21	3.00	1.65	4.03	–	–	33.67	0.57	12.86	13.26
Cr_2O_3	46.42	10.59	1.58	26.22	FeO^t	4.76	3.50	3.09	3.84	8.14	6.71	8.33	12.00	10.02	0.18	4.02	5.94	5.19
FeO^t	37.33	16.45	14.33	18.51	MnO	0.10	–	–	0.15	0.47	0.21	0.40	–	0.24	–	–	0.11	0.13
MnO	5.12	0.29	0.37	0.29	MgO	15.07	15.52	13.06	15.98	32.58	34.32	33.16	47.72	48.96	–	21.93	16.14	17.09
MgO	0.77	17.37	18.70	14.03	CaO	22.40	23.03	24.47	21.16	0.78	0.44	0.87	–	–	15.78	13.69	12.09	11.87
CaO	0.27	–	–	–	Na_2O	0.43	0.11	0.64	0.45	–	–	–			2.93	–	4.04	3.00
					K_2O										–	–	–	–
					Cr_2O_3	0.80	0.56	1.09	0.28	0.46	0.38	0.17				–	1.03	0.61
					NiO					0.13	–		0.45	0.25				
Total	*96.73*	*98.87*	*99.80*	*99.33*	*Total*	*100.11*	*100.10*	*98.56*	*99.81*	*100.77*	*100.27*	*100.72*	*100.45*	*100.09*	*100.33*	*98.07*	*98.12*	*97.36*
Structural formula on the basis of 4 O Spinel and Olivine, 6 O Pyroxene, 8O Plagioclase, 23 O Amphibole																		
Si	0.010	0.004	0.007	–	Si	1.877	1.872	1.849	1.861	1.909	1.944	1.862	0.993	0.996	2.183	7.944	6.056	6.209
Ti	0.079	–	0.002	0.007	Ti	0.022	0.030	0.025	0.017	0.006	0.006	0.008	–	–	–	–	0.413	0.304
Al	0.164	1.711	1.931	1.356	Al^{IV}	0.123	0.128	0.151	0.139	0.091	0.056	0.138	–	–	1.813	0.056	1.944	1.791
Cr	1.367	0.225	0.032	0.599	Al^{VI}	0.076	0.083	0.102	0.128	0.032	0.011	0.027				0.037	0.237	0.445
Fe^{3+}	0.206	0.049	0.000	0.042	Fe^{3+}	0.016	0.000	0.019	0.000	0.053	0.032	0.136			0.007	0.005	0.000	0.048
Fe^{2+}	0.927	0.318	0.305	0.401	Fe^{2+}	0.130	0.107	0.077	0.117	0.182	0.161	0.104	0.247	0.205		0.456	0.717	0.573
Mn	0.162	0.007	0.008	0.007	Mn	0.003	–	–	0.005	0.014	0.006	0.012	–	0.005	–	0.008	0.014	0.016
Mg	0.043	0.696	0.708	0.602	Mg	0.824	0.843	0.726	0.867	1.685	1.766	1.720	1.754	1.789	–	4.488	3.460	3.644
Ca	0.011	–	–	–	Ca	0.881	0.899	0.978	0.826	0.029	0.016	0.032	–	–	0.773	2.014	1.864	1.820
					Na	0.030	0.008	0.046	0.032	–	–	–			0.259	–	1.126	0.832
					K										–	–	–	–
					Cr	0.023	0.016	0.032	0.008	0.013	0.010	0.005				–	0.117	0.069
					Ni					0.004	–		0.009	0.005				
	2.967	3.010	2.992	3.013		4.005	3.986	4.006	4.000	4.017	4.010	4.043	3.003	3.001	5.039	15.001	15.948	15.750
Cr#	89.3	11.6	1.6	30.6	Mg#	84.9	88.8	88.3	88.1	87.7	90.1	87.6	87.6	89.7		90.7	82.9	85.4

(*continued on next page*)

Table 2 (*continued*)

	(J) Spinel					(K) Clinopyroxene				(L) Orthopx			(M) Olivine		(N) Pl	(O) Amph		
	GG3	MR1		MR3		GG2	MR1	MR3	MR10	MR1	MR3	MR10	MR1	MR3	MR1	MR1	MR1	MR10
																Trm	Ti-Prg	Ti-Prg
Mg#	3.5	65.3	69.9	57.5														
Sp	4.2	69.2	71.1	59.9	Wo	47.9	48.6	54.7	45.6	1.5	0.8	1.7						
Mg-Chr	0.0	0.0	0.0	0.0	En	44.8	45.6	40.6	47.9	88.0	90.3	90.4						
Mg-Fer	0.0	0.0	0.0	0.0	Fs	7.3	5.8	4.8	6.5	10.5	8.8	7.9						
Hrc	3.9	15.9	25.8	7.6	Fo								87.6	89.5				
Chr	67.9	11.2	1.6	29.8	Fa								12.4	10.5				
Usp	12.2	0.6	0.7	0.7	An										74.9			
Mt	11.8	3.0	0.8	2.1	Ab										25.1			
					Kfs										0.0			

FeO^t = total iron; –, below detection limit; blank, not analysed. *, core of vesuvianite; 1, H_2O calculated following Barriga and Fyfe (1983). Chlorite of GG also contains Cl up to 1.15 wt.% and SO_3 up to 0.84 wt.%; serpentine of MR SO_3 up to 0.25 wt.%. Fe^{3+} in garnet calculated from Deer et al. (1992) [Droop (1987)]; Fe^{3+} in amphibole calculated following Hawthorne et al. (2012). Mg# = 100*Mg/(Mg + Fe); Cr# = 100*Cr/(Cr + Al). End member calculation for garnet following Barriga and Fyfe (1983). Uvr = uvarovite, And = andradite, Pyr = pyrope, Sps = spessartine, Hgr = hydrogarnet, Grs = grossular, Alm = almandine, Sch = schorlomite, Prh = prehnite, Pmp = pumpellyite, Ilm = ilmenite, Wo = wollastonite, En = enstatite, Fs = ferrosilite, Sp = spinel, Chr = chromite, Fer = ferrite, Hrc = hercynite, Usp = ulvospinel, Mt = magnetite, Pl = plagioclase, Amph = amphibole, Fo = forsterite, Fa = fayalite, An = anorthite, Ab = albite, Kfs = K-feldspar, Trm = tremolite, Prg = pargasite.

spectral zone of the O–H stretching modes has a non-homogeneous behaviour, sometimes with a low intensity band either between 3500 and 3600 cm^{-1} or between 3650 and 3750 cm^{-1} (Fig. 5c). The GG samples differ significantly from the MR ones. In fact, the band of O–H stretching modes has a much greater intensity and is centered approximately at 3650 cm^{-1} (Fig. 5d), thus suggesting the presence of hydrogrossular component in garnet (Kolesov and Geiger, 2005). The triplet of the Si–O stretching is less defined and highlights the contribution of the grossular component to andradite (Kolesov and Geiger, 2005) (Fig. 5d).

Raman maps of the prismatic crystals of GG vesuvianite, showing a cribrous core and a fresh rim (see above), evidence that the crystals are made up of a garnet core (mixture of andradite and grossular) rounded by a vesuvianite rim (Fig. 6). These features support the reaction of progressive replacement of garnet by vesuvianite.

5.4. Whole-rock chemistry

The whole rock chemistry of selected samples is reported in Table 3. The studied rodingites are Si-poor and Mg- and Ca-rich. MR1 and MR3 have high MgO contents, whereas GG1-2-3, MR4 and MR6 samples exhibit higher CaO and Al_2O_3 combined with lower MgO contents, in agreement with their derivation from peridotitic and pyroxenitic protoliths, respectively (see Table 1). The highest content of CaO shown by sample MR15 is due to the widespread presence of garnet with grossular composition.

Whole rock compositions of the investigated rodingites are plotted in the ACF diagram (Fig. 7), together with rodingites from the literature. The rodingites of Groppo di Gorro have homogenous composition, suggesting that the metasomatic transformations have extensively involved the original rock with widespread formation of vesuvianite, diopside, calcite, garnet and chlorite. On the other hand, hydrothermal/metasomatic processes affecting the Mt. Rocchetta-Campeggi mantle bodies led to formation of rocks characterized by variable degree of serpentinization containing diopside and rare garnet (samples MR1, MR3 and MR4), moderately metasomatized rocks with garnet, diopside, serpentine and rare vesuvianite (sample MR6), up to strongly metasomatized rocks (sample MR15), consisting of dominant garnet + chlorite + diopside ± vesuvianite. As a result, the compositions are quite variable and the samples are distributed along a trend pointing towards the garnet composition and supporting different degrees of metasomatism (Fig. 7).

The REE patterns of the rodingites (Fig. 8) show negatively fractionated LREE and nearly flat MREE and HREE. Samples MR1 and MR3 have the lowest REE abundances with a slight Eu negative anomaly in sample MR1. The highest amount of REE, particularly MREE and HREE, has been observed in sample MR6. Samples MR4 and MR15 exhibit similar patterns, with small Eu negative anomalies and a slight depletion of HREE in sample MR15. Profiles of GG samples overlap each other with the exception of sample GG1 due to the slightly more negatively fractionated LREE.

Comparing the rodingite samples with their alleged protoliths, we observe that GG samples have REE patterns very similar to the pyroxenite GAV2, with a slight enrichment in HREE (Fig. 8). Samples MR1 and MR3 are significantly depleted in LREE and MREE with respect to the peridotite CAM2, while HREEs overlap. Samples MR4 and MR15 have enriched LREE and depleted HREE patterns compared to the pyroxenite CAM8. The pattern of sample MR6 is considerably enriched in all the REEs compared to CAM8 (Fig. 8).

5.5. Fluid inclusions

Primary fluid inclusions occur in diopside and garnet from MR and in calcite and diopside from GG. In the thin prismatic vesuvianite, fluid inclusions are scarce and tiny. Fluid inclusions in diopside are abundant and elongated according to c-axis of the prismatic crystals whereas inclusions with other shapes are rare. The size of the inclusions is variable from less than 1 μm to 2–14 μm. In garnet, fluid inclusions are up to 1 μm

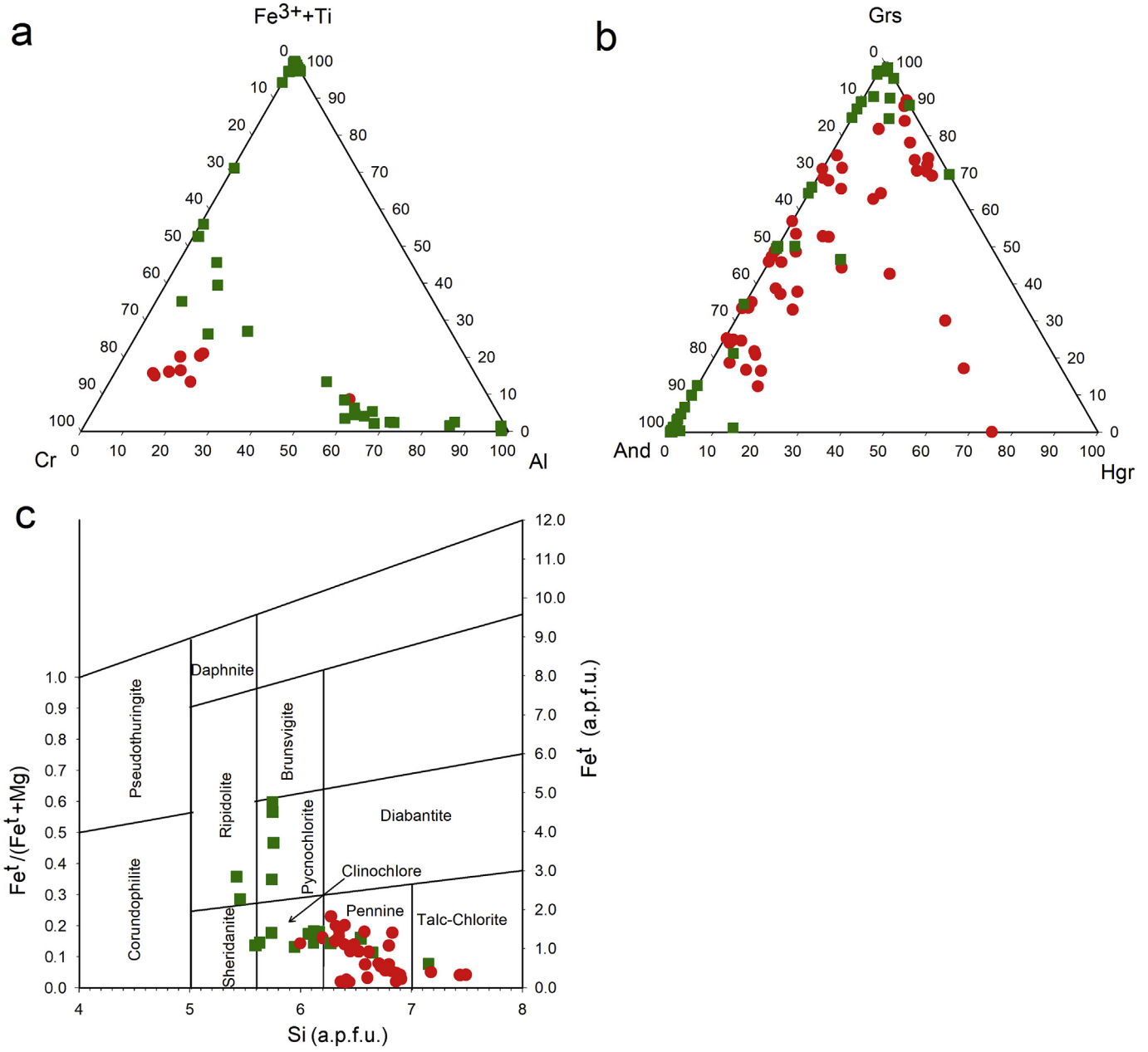

Fig. 4. (a) Ternary diagram of oxide minerals; (b) Ternary diagram Hydrogrossular (Hgr) – Grossular (Grs) – Andradite (And) of the analysed garnets; (c) Plot of the analysed chlorite in their classification diagram (after Hey, 1954). Symbols: red circle, Groppo di Gorro; green square, Mt Rocchetta.

and with irregular shape. Fluid inclusions in calcite of GG are relatively large (up to 19 μm) and show triangular-like shape. Regardless of the trapping mineral, fluid inclusions are two-phase inclusions with quite constant Vapour/Liquid ratio (V/L = 0.2–0.4).

Few microthermometric measures were performed owing to the generally small size of the fluid inclusions. The eutectic temperature Te, corresponding to the first phase variation, is in the range −19.9 to −21 °C, which suggests the presence of dissolved NaCl in water. The remaining solid phase melts in the range −2.8 to −0.6 °C (ice melting temperature Tm_{ice}). Fluid inclusions are CO_2-free. Nevertheless, the presence of small amount of CO_2 (not detectable by microthermometric measurement) cannot be excluded at GG due the presence of small amount of calcite in the rodingite association. Based on ice melting temperature, the total salinity, calculated with the software package of Bakker and Brown (2003) and the equation of Zhang and Frantz (1987), is in the range 0.5–2.9 wt.% NaCl. Microthermometric data on fluid inclusions from rodingites of different localities provided salinity values between 1.5 and 8 wt.% NaCl (Schandl et al., 1990; O'Hanley et al., 1992; Mittwede and Schandl, 1992; O'Hanley, 1996).

The total homogenization temperature (Th_{tot}) to liquid state occurs in the range 258–292 °C for Groppo di Gorro and 228–284 °C for Mt. Rocchetta, and they are comparable with the bibliographic data (196–290 °C; Mittwede and Schandl, 1992; O'Hanley, 1996; O'Hanley et al., 1992; Schandl et al., 1990). Rodingite formation generally occurs at shallow conditions ($P < 1$ kbar) and, for this reason, we calculated the trapping temperature for pressure values of 500 bar and 1 kbar. The resulting temperatures, obtained with the software package of Bakker and Brown (2003) and the equation of state of Knight and Bodnar (1989) and Bodnar and Vityk (1994), are in the range 297–334 °C (500 bar) and 337–380 °C (1 kbar) for GG, 264–327 °C (500 bar) and 300–373 °C (1 kbar) for MR.

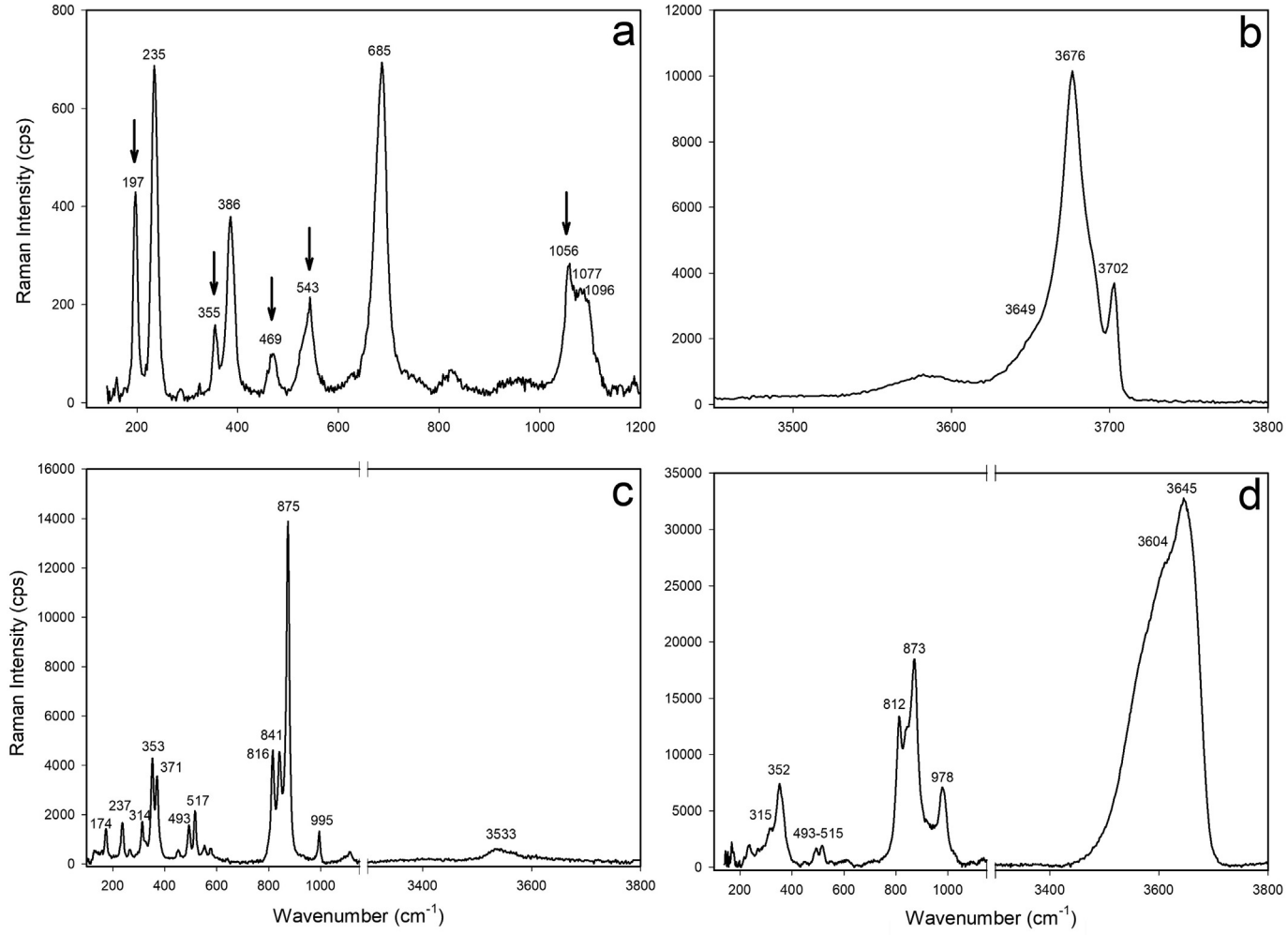

Fig. 5. Raman spectra of: (a) lizardite partially transformed in chlorite (see Fig. 3o), whose peaks are marked with an arrow; (b) peaks of lizardite in OH-stretching region (see Fig. 3o); (c) and (d) low- and high-frequency spectra of garnets of the rodingites from Mt. Rocchetta and Groppo di Gorro, respectively.

5.6. Mass balance calculations

The chemical variations of the protoliths during the metasomatic process have been evaluated by mass balance calculations (Venturelli et al., 1997) and with the method of isocone (Grant, 1986) considering Al as immobile element. The mass balance calculations were performed on anhydrous basis. A quantitative estimate of mass gain and loss of the chemical components and of the volume variations during metasomatic process are reported in Table 4 and Fig. 9, where the immobile element (Al) lies on the straight-line 0 value.

If compared to the pyroxenite of Mt. Gavi (GAV2), samples GG2 and GG3 show similar distribution with mass gain for all major elements, Sc, V, Co, Y and REE (Fig. 9a). Sample GG1 is slightly different due to the loss of Fe_2O_3, Ni, LREE (La, Ce, Pr) masses in addition to Cr and Zr mass loss which is higher than in the other samples (Table 4 and Fig. 9a). The metasomatic process giving the GG rodingite implies a slight increase in volume (from 22% up to 40%).

For Mt. Rocchetta, mass balance calculations have been performed on the rodingite samples MR1, MR3, MR4B, MR6A and MR15. Samples MR1 and MR3 were compared with the peridotite CAM2 (Table 4 and Fig. 9b). The two samples are similar and do not differ significantly from the protolith CAM2. The main difference is the mass gain of Cu (+3.58) shown by sample MR1. The other samples (MR4, MR6, MR15) were compared with the pyroxenite CAM8 (Table 4 and Fig. 9c). Sample MR15 shows mass loss for all the elements while sample MR6 shows mass loss of Na_2O and Sr and mass gain for all the other elements, particularly TiO_2 (1.76), Pr (1.89), Nd (1.73), MREEs (1.08–2.68) and HREEs (1.34–1.73). Sample MR4 shows intermediate character with mass gain of TiO_2, Fe_2O_3, MnO, MgO, Cr, Zr, LREE (except La) and loss of FeO, CaO, Co, Ni, Cu, Ga, Sr and La. All these features could be explained with the formation of grossular garnet in sample MR15, andradite in MR6 and abundant serpentine and diopside in MR4. The calculated increase of volume of MR rodingite is in the range 9%–37% with the exception of sample MR15 which shows a volume loss (−36%) (Table 4).

The volume variations calculated for Groppo di Gorro and Mt. Rocchetta is closely related to the present rodingite paragenesis. At GG and, occasionally, MR (sample MR6), the significant volume increase is likely related to the high abundance of hydrous phases chlorite, hydrogarnet and vesuvianite. In the sample MR15, garnet, with grossular and andradite molecules, is the only mineral of the rodingite assemblage; this is consistent with the observed loss of volume.

6. Discussion

6.1. The rodingitization process

Petrography, mineralogy and geochemistry of the investigated rocks highlight the great complexity of their origin and evolution due to high temperature processes (Müntener and Piccardo, 2003; Piccardo et al., 2004) and relatively high temperature polyphasic metasomatism.

The variable mineral assemblages found in the rodingites (diopside + vesuvianite + garnet + calcite + chlorite at GG; garnet + diopside +

Table 3
Whole rock analyses of rodingites from Groppo di Gorro (GG) and Mt. Rocchetta (MR), and their inferred protoliths (CAM2 = Campeggi peridotite; CAM8 = Campeggi pyroxenite; GAV2 = Mt. Gavi pyroxenite).

	GG1	GG2	GG3	MR1	MR1 vein	MR3	MR4	MR4 vein	MR 6	MR 15	MR 21	CAM 2	CAM 8	GAV2*
Major elements(wt.%)														
SiO_2	39.72	39.88	39.36	38.91	37.63	40.53	36.92	44.69	42.66	38.46	38.74	40.61	44.95	38.04
TiO_2	0.25	0.25	0.26	0.08	0.04	0.10	0.41	0.02	0.57	0.35	0.01	0.15	0.29	0.23
Al_2O_3	10.48	9.16	9.52	2.68	3.13	2.68	9.40	3.35	7.89	17.15	2.29	3.24	11.05	12.77
Fe_2O_3	1.38	2.62	2.73	3.79	4.46	2.02	2.48	1.12	1.46	1.19	5.59	3.77	1.33	2.22
FeO	5.30	4.00	3.90	2.80	3.60	5.60	2.60	1.20	4.80	1.60	2.90	4.70	4.10	4.30
MnO	0.15	0.12	0.12	0.12	0.06	0.12	0.15	0.13	0.15	0.07	0.07	0.13	0.15	0.12
MgO	21.83	21.99	22.47	36.56	36.54	38.99	29.94	30.04	21.53	11.51	37.01	35.51	18.05	22.01
CaO	12.25	13.08	12.67	1.15	0.71	2.58	6.94	11.28	14.07	24.06	1.17	2.79	15.37	11.38
Na_2O	0.19	0.32	0.32	0.14	0.23	0.13	0.17	0.18	0.15	0.15	–	0.07	0.33	0.14
K_2O	0.04	0.01	0.03	–	0.02	0.04	–	–	–	–	–	–	0.03	0.08
P_2O_5	–	–	–	–	–	–	–	–	–	–	–	–	–	–
LOI	6.99	6.77	7.17	12.58	12.34	5.68	9.80	7.37	5.75	4.27	12.07	8.82	4.09	8.46
Total	*99.17*	*98.64*	*98.98*	*99.12*	*99.16*	*99.09*	*99.10*	*99.50*	*99.02*	*98.99*	*99.85*	*99.78*	*99.74*	*99.75*
Trace elements and REEs(ppm)														
Sc	39	28	30	12	1	11	42	2	36	47	5	13	46	17
Be	–	–	–	–	–	–	–	–	–	–	–	–	–	
V	143	113	114	31	19	39	141	17	241	162	11	73	186	115
Cr	1070	1460	1820	1990	60	1890	2240	90	1290	560	320	2350	1320	2570
Co	42	54	51	60	35	81	27	13	49	14	104	92	41	53
Ni	480	710	700	1240	620	1340	480	270	760	140	1650	1710	720	900
Cu	60	40	50	40	–	10	10	–	70	–	–	10	100	
Zn	40	50	50	50	–	50	40	–	40	–	–	50	–	
Ga	4	5	6	2	2	3	4	4	7	6	3	3	7	
Ge	–	1	–	–	–	–	–	–	–	–	–	–	–	
As	–	–	–	–	–	–	–	–	–	–	–	–	–	
Rb	–	–	–	–	–	–	–	–	–	–	–	–	–	
Sr	3	3	9	–	2	4	2	–	13	–	3	4	316	15
Y	8	6	7	3	–	–	11	–	15.2	8	–	3	13	4.9
Zr	5	8	6	–	–	–	18	–	13	11	–	8	13	10
Nb	–	–	–	–	–	–	–	–	–	–	–	–	–	
Mo	–	–	–	–	–	–	–	–	–	–	–	–	–	
Ag	–	–	–	–	–	–	–	–	0.8	–	–	–	–	
In	–	–	–	–	–	–	–	–	–	–	–	–	–	
Sn	4	4	6	2	4	8	4	10	–	4	–	–	–	
Sb	–	–	–	–	–	–	–	–	0.6	–	–	–	–	
Cs	–	–	–	–	–	–	–	–	0.5	–	0.3	–	0.8	
Ba	3	–	–	–	5	10	–	–	–	–	–	–	8	
La	0.2	0.3	0.3	–	–	0.1	0.3	–	0.6	0.4	0.31	0.4	0.6	0.37
Ce	0.7	1.2	1.1	0.3	–	0.4	1.5	–	1.72	1.4	0.81	0.7	1.2	1.4
Pr	0.14	0.21	0.21	0.06	–	0.08	0.32	–	0.55	0.31	0.29	0.12	0.26	0.22
Nd	1.1	1.4	1.4	0.4	–	0.5	2.4	–	3.2	2.2	1.44	0.8	1.6	1.26
Sm	0.5	0.6	0.6	0.2	–	0.2	1	–	2.17	0.8	0.76	0.3	0.9	0.48
Eu	0.28	0.29	0.26	0.07	–	0.09	0.32	–	0.916	0.27	0.308	0.12	0.34	0.226
Gd	0.8	0.8	0.8	0.3	–	0.3	1.4	–	2.67	1.1	0.51	0.4	1.3	0.74
Tb	0.2	0.2	0.2	–	–	–	0.3	–	0.52	0.2	0.09	–	0.3	0.13
Dy	1.2	1.1	1.1	0.4	–	0.4	1.9	–	3.41	1.5	0.58	0.6	2	0.92
Ho	0.3	0.2	0.2	0.1	–	–	0.4	–	0.76	0.3	0.13	0.1	0.5	0.19
Er	0.8	0.7	0.7	0.3	–	0.3	1.2	–	2.23	0.9	0.49	0.4	1.3	0.52
Tm	0.12	0.11	0.1	–	–	–	0.18	–	0.384	0.13	0.103	0.05	0.21	0.078
Yb	0.8	0.7	0.6	0.3	–	0.3	1.2	–	2.8	0.8	0.8	0.3	1.4	0.56
Lu	0.13	0.11	0.1	0.05	–	0.05	0.19	–	0.414	0.11	0.134	0.05	0.24	0.09
Hf	0.3	0.3	0.3	–	–	–	0.7	–	1.8	0.3	0.8	–	0.3	0.3
Ta	–	–	–	–	–	–	–	–	0.18	–	0.14	–	–	
W	–	–	–	–	–	–	–	–	1.2	2	0.9	–	–	
Tl	–	–	–	–	–	–	–	–	0.13	–	–	–	–	
Pb	–	–	–	–	–	–	–	–	–	–	–	–	–	
Bi	–	–	–	–	–	–	–	–	–	–	–	–	–	
Th	–	–	–	–	–	–	–	–	0.21	–	0.17	0.1	–	
U	–	–	–	–	–	–	–	–		–	0.13	–	–	

Data from * Montanini et al. (2017). FeO calculated by titration. Blank, not analysed; –, below detection limit.

serpentine ± vesuvianite ± prehnite ± chlorite ± pumpellyite at MR) also indicate that the metasomatism followed different chemical reaction sequences in the two outcrops (Table 5).

The absence of brucite suggests that the serpentinization of olivine was related to silica-rich fluids (high $aSiO_2$) according to the reaction

$$3\ Fo + SiO_2\ (aq) + 4\ H_2O = 2\ Srp1 \quad (1)$$

Serpentinization of both ortho- and clinopyroxene is frequently observed. Since the serpentinization of the pyroxenes gives silica-rich fluids according to the reactions

$$3\ Cpx + 6\ H^+ = Srp1 + 3\ Ca^{2+} + 4\ SiO_2\ (aq) + H_2O \quad (2a)$$

$$3\ Opx + 4\ H_2O = 2\ Srp1 + 2\ SiO_2\ (aq) \quad (2b)$$

we infer that a unique fluid cannot be responsible for the

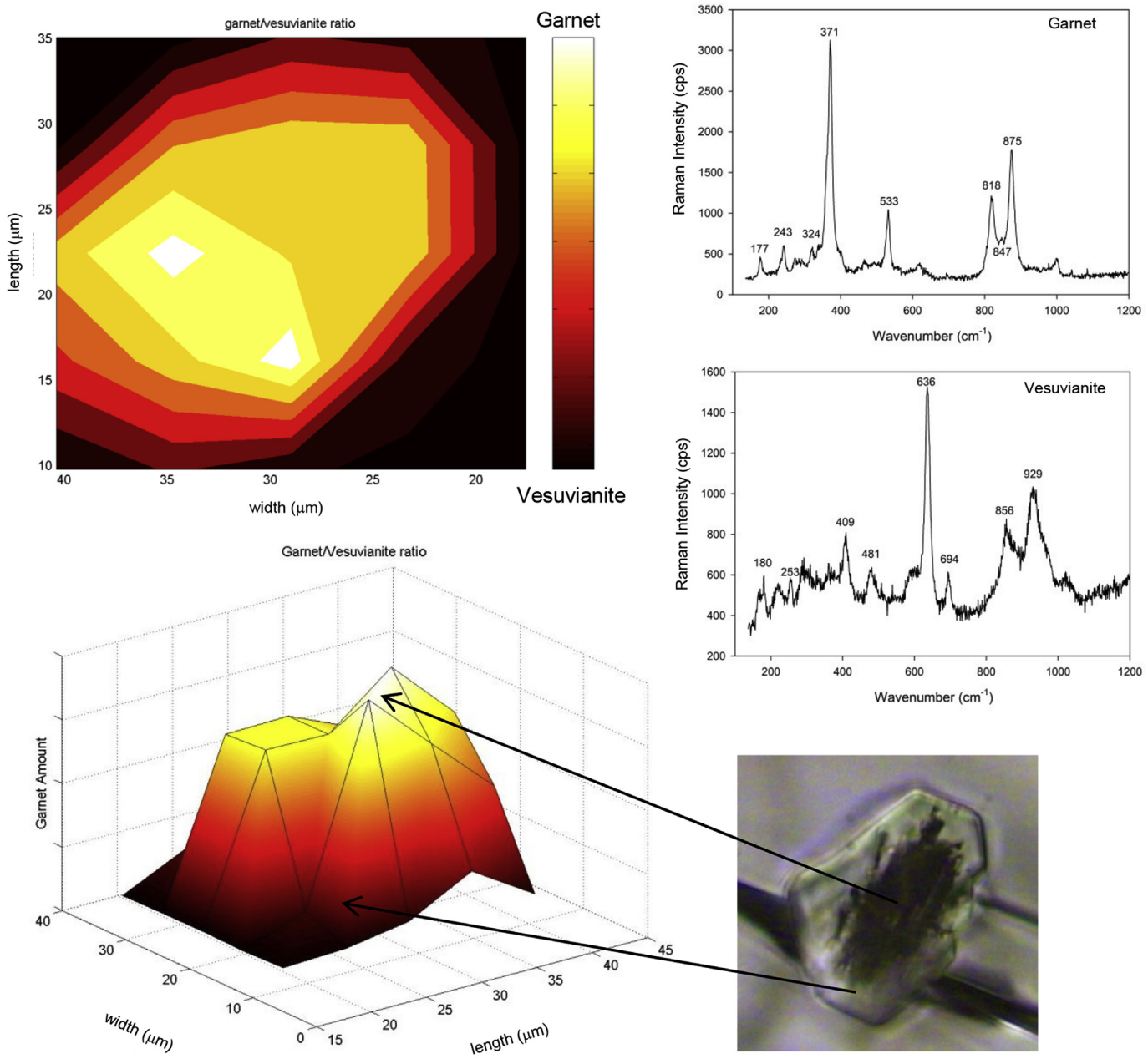

Fig. 6. Two-dimensional and three-dimensional Raman maps of vesuvianite with a cribrous core (Groppo di Gorro).

serpentinization of all the primary phases of the investigated rocks and that serpentinization may have occurred in successive steps.

The serpentine of GG samples is totally replaced by pseudomorphic chlorite whereas an incipient chloritization of serpentine in MR samples is shown by micro-Raman spectroscopy (Fig. 5a). The formation of chlorite implies the availability of aluminium, whose source could be the alteration of plagioclase according to reaction

$$5\ \mathrm{Srp1} + 3\ \mathrm{Pl} + 6\ \mathrm{H^+} = 3\ \mathrm{Chl1} + 3\ \mathrm{Ca^{2+}} + 7\ \mathrm{SiO_2\ (aq)} + \mathrm{H_2O} \quad (3)$$

with increase of Ca and silica activity in the released fluids.

The beginning of the rodingitization process coincides with the appearance of grossular/hydrogrossular. At Groppo di Gorro, garnet may derive from the breakdown of plagioclase (crystallized around spinel relics) and clinopyroxene according to the reactions

$$2\ \mathrm{Pl} + 5\ \mathrm{Cpx} + \mathrm{H_2O} + 8\ \mathrm{H^+} = \mathrm{Hgr} + \mathrm{Chl2} + 4\ \mathrm{Ca^{2+}} + 8.5\ \mathrm{SiO_2\ (aq)} \quad (4)$$

$$\mathrm{Pl} + 2\ \mathrm{Ca^{2+}} + 3\ \mathrm{H_2O} + 0.5\ \mathrm{SiO_2\ (aq)} = \mathrm{Hgr} + 4\ \mathrm{H^+} \quad (5a)$$

At Mt. Rocchetta, the appearance of grossular/hydrogrossular is associated with fine-grained aggregates of chlorite, rare prehnite and pumpellyite, which support the reactions proposed by Coleman (1967).

$$\mathrm{Pl} + \mathrm{Ca^{2+}} + \mathrm{SiO_2\ (aq)} + 2\ \mathrm{H_2O} = \mathrm{Prh} + 2\ \mathrm{H^+} \quad (5b)$$

$$\mathrm{Prh} + \mathrm{Ca^{2+}} + \mathrm{H_2O} = \mathrm{Hgr} + 2\ \mathrm{H^+} + 0.5\ \mathrm{SiO_2\ (aq)} \quad (5c)$$

The Ca^{2+} ions for the formation of hydrogarnet are provided by both plagioclase and clinopyroxene. The reaction involving clinopyroxene gives pumpellyite as intermediate product (Koutsovitis et al., 2018).

The formation of diopside at the expense of garnet occurs in a second stage of the metasomatic process according to the reaction

$$\mathrm{Hgr} + 6\ \mathrm{Mg^{2+}} + 3.5\ \mathrm{SiO_2\ (aq)} + 9\ \mathrm{H_2O} = \mathrm{Di} + \mathrm{Chl2} + 2\ \mathrm{Ca^{2+}} + 12\ \mathrm{H^+} \quad (6)$$

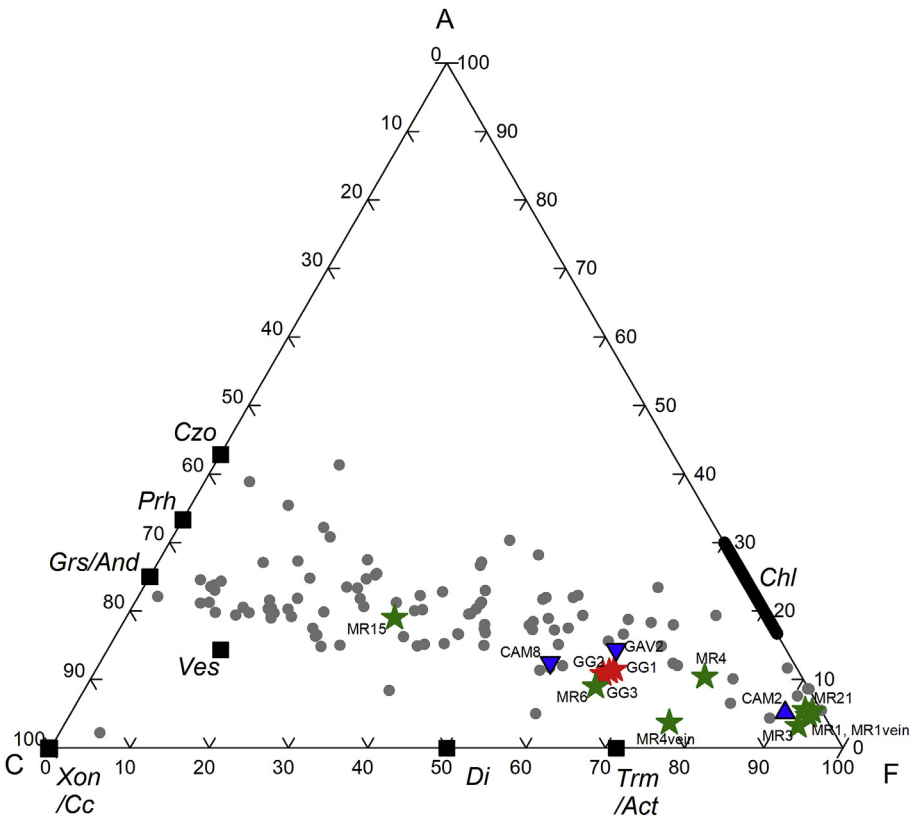

Fig. 7. ACF diagram (A = Al_2O_3+Fe_2O_3–Na_2O–K_2O, C═CaO, F═FeO + MnO + MgO) of the investigated rodingites (red star, Groppo di Gorro; green star, Mt. Rocchetta) and of the protoliths (blue symbols: down triangle, pyroxenites from Campeggi and from Mt. Gavi; up triangle, peridotite from Campeggi). For comparison, rodingites associated to ophilites from various localities (Coleman, 1967; Capedri et al., 1978; Schandl et al., 1989; O'Hanley et al., 1992; Dubińska, 1997; Hatzipanagiotou and Tsikouras, 2001; Hatzipanagiotou et al., 2003; Pomonis et al., 2008; Austrheim e Prestvik, 2008; Tsikouras et al., 2009; Tsikouras et al., 2013) are also plotted. Grs/And, grossular/andradite; Prh, prehnite; Czo, clinozoisite; Ves, vesuvianite; Di, diopside; Trm/Act, tremolite/actinolite; Chl, chlorite; Xon, xonotlite; Cc, calcite.

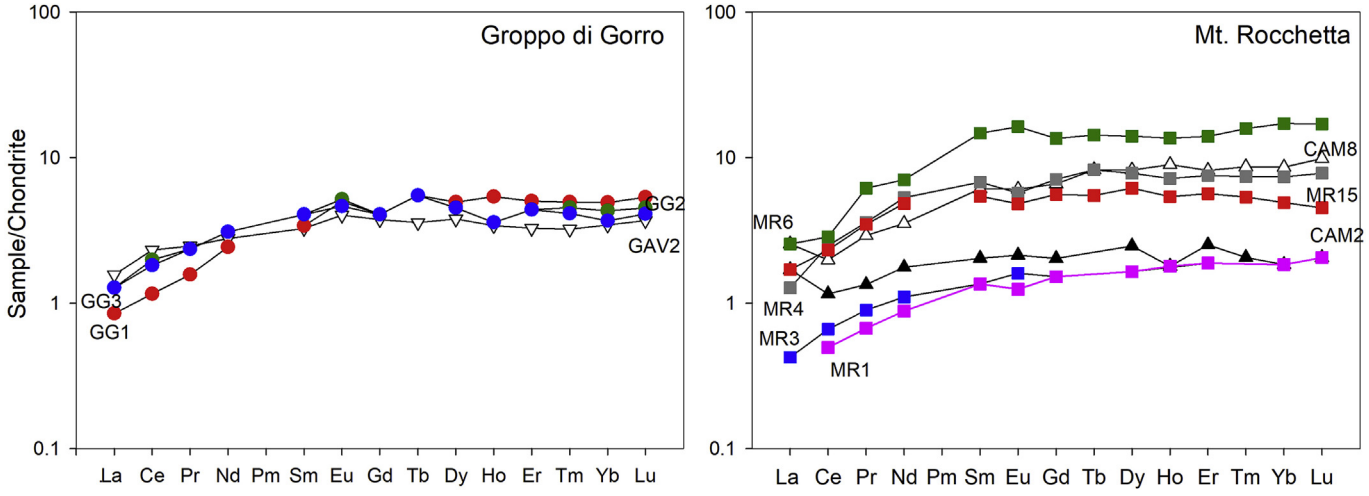

Fig. 8. REE patterns of the rodingites from Groppo di Gorro (circle: red GG1, green GG2, blue GG3) and Mt. Rocchetta (square: pink MR1, blue MR3, grey MR4, green MR6, red MR15, white MR21) compared to pyroxenite of Mt. Gavi (down white triangle) and to peridotite and pyroxenite of Campeggi (up black and white triangle, respectively). The chondritic data are from Anders and Grevesse (1989) for REEs and from Sun (1982) for transition elements.

where the metasomatic fluid is magnesium- and silica-rich as suggested by Hatzipanagiotou et al. (2003).

At GG, the overgrowth of chlorite on garnet and diopside (Fig. 3a) suggests the decomposition of the first rodingite association (Koutsovitis et al., 2013), according to the reaction

$$Grs + 5\ Di + 4\ H_2O + 8\ CO_2 = 8\ Cc + Chl2 + 10\ SiO_2\ (aq) \quad (7)$$

The usual association of vesuvianite with diopside indicates that both minerals are involved in the final metasomatic stage. Raman maps show that the vesuvianite forms from garnet (Fig. 6), as also suggested by Dubińska (1997). At GG vesuvianite crystallizes from garnet and calcite according to the reaction of Hatzipanagiotou and Tsikouras (2001).

$$5\ Grs + Di + Chl + 14\ Cc + 7\ SiO_2\ (aq) + 2\ H_2O = 3\ Ves + 14\ CO_2 \quad (8a)$$

Differently, at MR calcite is absent and vesuvianite crystallizes from garnet and diopside (Fig. 3f) according to the reaction of Li et al. (2007).

$$5\ Grs + Di + Chl + 14\ Ca^{2+} + 7\ SiO_2\ (aq) + 16\ H_2O = 3\ Ves + 28\ H^{+} \quad (8b)$$

Table 4
Elemental gain (+) and loss (−) as K_i-1, assuming Al immobile.

Precursor	CAM2		CAM8			GAV2		
Rodingite	MR1	MR3	MR4	MR6	MR15	GG1	GG2	GG3
SiO_2	0.158	0.207	−0.034	0.329	−0.449	0.272	0.461	0.388
TiO_2	−0.300	−0.158	0.669	1.757	−0.217	0.303	0.515	0.522
Fe_2O_3	0.215	−0.352	1.192	0.537	−0.424	−0.243	0.645	0.649
FeO	−0.280	0.440	−0.255	0.640	−0.749	0.502	0.297	0.219
MnO	0.105	0.152	0.183	0.354	−0.699	0.503	0.338	0.298
MgO	0.245	0.327	0.950	0.671	−0.589	0.208	0.393	0.369
CaO	−0.502	0.118	−0.469	0.282	0.009	0.312	0.602	0.493
Na_2O	1.418	1.245	−0.394	−0.363	−0.707	0.654	2.186	2.066
K_2O						−0.391	−0.826	−0.497
Sc	0.058	0.044	−0.0.1	0.069	−0.349	1.804	1.300	1.370
V	−0.513	−0.341	−0.171	0.770	−0.445	0.520	0.372	0.331
Cr	−0.030	−0.008	0.856	0.335	−0.730	−0.491	−0.207	−0.049
Co	−0.253	0.086	−0.280	0.632	−0.783	−0.031	0.422	0.292
Ni	−0.169	−0.034	−0.271	0.442	−0.876	−0.348	0.101	0.044
Cu	3.584	0.233	−0.891	−0.044				
Zn	0.146	0.233						
Ga	−0.236	0.233	−0.375	0.366	−0.454			
Sr		0.233	−0.993	−0.944		−0.755	−0.721	−0.194
Y	0.146		−0.074	0.597	−0.608	0.996	0.710	0.918
Zr			0.515	0.366	−0.461	−0.389	0.117	−0.194
La		−0.692	−0.453	0.366	−0.575	−0.339	0.132	0.089
Ce	−0.509	−0.295	0.367	0.958	−0.257	−0.389	0.197	0.055
Pr	−0.427	−0.178	0.346	1.889	−0.241	−0.222	0.333	0.282
Nd	−0.427	−0.229	0.641	1.731	−0.124	0.067	0.551	0.492
Sm	−0.236	−0.178	0.216	2.293	−0.434	0.273	0.745	0.678
Eu	−0.331	−0.075	0.030	2.679	−0.494	0.514	0.791	0.545
Gd	−0.140	−0.075	0.178	1.805	−0.461	0.322	0.509	0.451
Tb			0.094	1.367	−0.575	0.881	1.148	1.066
Dy	−0.236	−0.178	0.039	1.329	−0.522	0.594	0.669	0.605
Ho	0.146		−0.125	1.076	−0.618	0.930	0.470	0.413
Er	−0.140	−0.075	0.010	1.343	−0.559	0.881	0.879	0.807
Tm			−0.062	1.497	−0.606	0.881	0.969	0.721
Yb	0.146	0.233	−0.062	1.731	−0.636	0.746	0.745	0.439
Lu	0.146	0.233	−0.134	1.356	−0.708	0.766	0.706	0.492
ΔM (vol%)	14.6	23.3	9.4	36.6	−36.3	22.2	39.6	34.3

K_i-1 according to Venturelli et al. (1997), ΔM according to Grant (1986).

6.2. Thermodynamic modelling of the rodingite reactions

As shown by the suggested reactions (Table 5), the activity of Ca, Mg and silica and the pH of the solutions are fundamental to enhance the progress of the reactions. Thus, mass transfer is largely driven by the activities of Ca, Mg and Si of the serpentinizing fluids. According to Bach and Klein (2009), to understand how such compositional gradients can influence the fluid-mineral phase relations in rodingitization, a titration reaction path model was used. In this study, a generic basaltic composition (diopside 0.6 – anorthite 0.4; Morse, 1980) was added as solid reactant to serpentinizing fluids of seawater and of meteoric origin. The thermodynamic models of the reaction paths have been elaborated considering a temperature of 300 °C, that is the average of the temperatures estimated by the data on the fluid inclusions (264–380 °C) for pressures ≤ 1 kbar. These data are in the same range as those obtained from fluid inclusions and oxygen isotopes (Schandl et al., 1990; O'Hanley et al., 1992; Mittwede and Schandl, 1992).

Despite to the different composition and genesis of the two serpentinizing fluids chosen as initial composition, the reaction path modeling with basaltic composition produced similar activity paths (Fig. 10). In particular, according to Bach and Klein (2009) and Bach et al. (2013), the two fluids are within a discrete range of dissolved silica activity ($-3 < \log[SiO_2(aq)] < -6$) and calcium/hydrogen ion activity ratio ($7 < \log[Ca^{2+}/(H^+)^2] < 11.5$). Moreover, the range of the obtained magnesium/hydrogen ion activity ratio is $5 < \log[Mg^{2+}/(H^+)^2] < 8$ (Fig. 10). Assuming the above mentioned silica activity range, similar values of the calcium/ and magnesium/hydrogen ion activity ratios are obtained from the reactions 1–8 (Table 5, Supplementary Material S2).

The serpentinization and chloritization reactions (1–3 in Table 5), under equilibrium conditions and assuming $T = 300$ °C, consistent with the presence of lizardite as serpentine polymorph (Schwartz et al., 2013), have high negative values of ΔG°_r (−19.83/−49.27, see Supplementary Material S2), thus they spontaneously evolve towards the products.

The reactions of garnet formation (4, 5a–c, Table 5) have negative log K and high to very high positive values of ΔG°_r (from 56.89 to 294.93 kJ mol^{-1}). The reactions involving plagioclase (5a–c, Table 5) require a Ca^{2+}-rich solution ($\log[Ca^{2+}]/[H^+]^2 > 8.2/15.2$ for $\log[SiO_2(aq)] = -3$ or $\log[Ca^{2+}]/[H^+]^2 > 8.64/11.2$ for $\log[SiO_2(aq)] = -6$; Supplementary Material S2 and Fig. 10a) with pH decreasing. The breakdown of primary clinopyroxene (reaction 4, Table 5) produces garnet at high silica activity ($\log[SiO_2(aq)] > -2.3$; Supplementary Material S2 and Fig. 10a).

In the previous published rodingitization models (Bach and Klein, 2009; Bach et al., 2013), grossular was considered due to the lack of thermodynamic data on hydrogrossular. In our model, despite the insertion of hydrogrossular in the used dataset, the precipitation of grossular rather than hydrogrossular is obtained. This could be due to the considered average composition for hydrogrossular ($Ca_3Al_2Si_{0.82}O_{3.28}(OH)_{8.72}$) and the related thermodynamic data available from literature (Matschei et al., 2007; Dilnesa et al., 2014). Indeed, the composition of this mineral and its thermodynamic data can have a wide variability. Owing to these limits, in Fig. 10a hydrogrossular nucleation occurs only at low silica activity ($\log[SiO_2(aq)] < -6$) and log

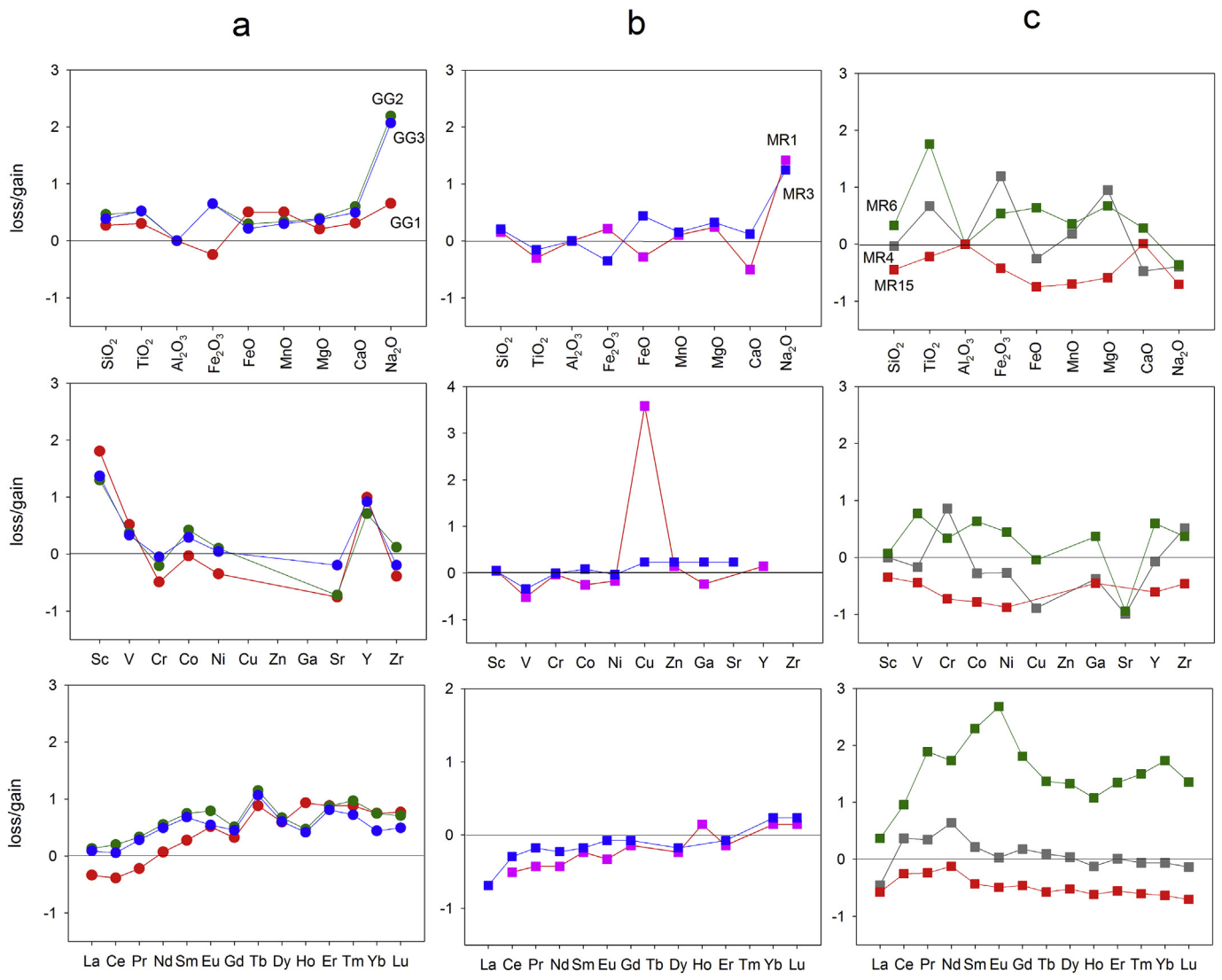

Fig. 9. Plots for major, trace and RE elements after mass balance calculations, using the method of Venturelli et al. (1997), assuming Al as immobile element during rodingite process. (a) GG rodingites (red GG1, green GG2, blue GG3), compared to pyroxenite of Mt. Gavi (GAV2). (b, c) MR rodingites, compared to peridotite CAM2 and pyroxenite CAM8, respectively (pink MR1, blue MR3, grey MR4, green MR6, red MR15). Positive values mean gain and negative values loss.

$[Ca^{2+}/(H^{+})^2] > 12$, as suggested by literature (Beard and Hopkinson, 2000, and references therein), which is quite higher than in the starting fluid composition. However, buffering the concentration of aqueous silica by hydrogrossular under the P-T condition of the described model ($T = 300$ °C, $P = 1$ kbar), in the activity diagram the fields of hydrogrossular and hydrogarnet appear for high $\log[Ca^{2+}/(H^{+})^2]$ and low silica activity (Fig. 10a), as suggested by Beard and Hopkinson (2000) and Li et al. (2004).

The diopside formation (reaction 6) requires addition of Mg^{2+} (log $[Mg^{2+}]/[H^{+}]^2 > 5.2$ for $\log[SiO_2(aq)] = -3$ and $\log[Mg^{2+}]/[H^{+}]^2 > 8.3$ for $\log[SiO_2(aq)] = -6$; Supplementary Material S2). In the presence of vesuvianite, diopside is formed in a reduced range of Ca and Mg activities for higher silica activity ($\log[SiO_2(aq)] = -3$); on the contrary, when the vesuvianite is absent, diopside precipitates more easily and in a greater range of silica activity (Fig. 10).

The breakdown of garnet and diopside to form calcite at GG (reaction 7, Table 5) requires a CO_2 fugacity from $10^{-0.3}$ to $10^{-4.1}$ with increasing of aqueous silica activity (10^{-6} to 10^{-3}) (see Supplementary Material S2). Calcite is formed only by meteoric fluids and only in the first stage of the reaction progress (>0.08) (Supplementary Material S3). The carbonation reaction can be attributed to infiltration of hydrothermal fluids with relatively high Ca^{2+}/Mg^{2+} and CO_2/H_2O ratios with mildly oxidizing conditions from less deep crustal levels (Beard and Hopkinson, 2000; Koutsovitis et al., 2013).

The vesuvianite can form spontaneously through the reaction 8a and 8b because they have a negative or slightly positive values of ΔG°_r ($\Delta G^{\circ}_r = -28.37$ and 16.82, respectively). The reaction (8b) in MR needs a small amount of Ca^{2+} (Supplementary Material S2) and reaction (8a) in GG proceeds at any CO_2(g) fugacity value. Therefore, the formation of vesuvianite does not necessarily require a fluid phase with very low CO_2 activity (Rice, 1983; Galuskin et al., 2003). This agree with the composition of serpentinizing fluid, which usually contain abiogenic reduced carbon as CH_4 instead of CO_2 (Boschetti et al., 2013b, 2013a). Anyway, the appearance of vesuvianite is favored by an increase of Ca activity and mildly low silica activity (Fig. 10a).

According to the previous published rodingitization models (Bach and Klein, 2009; Bach et al., 2013), almost all fluids obtained from the modeling show the formation of tremolite (Supplementary Material S3). If vesuvianite precipitation is achieved, the Ca–OH meteoric-derived fluid starts to precipitate tremolite at the first stage of reaction progress (0.01), whereas the Na–Cl seawater-derived fluid approximatively at the middle (0.3). Considering the lack of tremolite in the studied rodingite paragenesis, we can deduce that (i) it was back reacted to form new phases or (ii) reaction progress stopped before its precipitation. First

Table 5
Mineral reactions.

Minerals	Chemical formula	Abbreviations
Forsterite	Mg_2SiO_4	*Fo*
Clinopyroxene, Diopside	$CaMgSi_2O_6$	*Cpx, Di*
Orthopyroxene	$Mg_2Si_2O_6$	*Opx*
Serpentine	$Mg_3Si_2O_5(OH)_4$	*Srp*
Plagioclase	$CaAl_2Si_2O_8$	*Pl*
Chlorite	$Mg_5Al(AlSi_3O_{10})(OH)_8$	*Chl*
Hydrogrossular	$Ca_3Al_2Si_{2.5}O_{10}(OH)_2$	*Hgr*
Grossular	$Ca_3Al_2Si_3O_{12}$	*Grs*
Prehnite	$Ca_2Al_2Si_3O_{10}(OH)_2$	*Prh*
Vesuvianite	$Ca_{10}Mg_2Al_4(SiO_4)_5(Si_2O_7)_2(OH)_4$	*Ves*
Mineral reactions		
Serpentinization		
(1) 3 Fo + SiO_2 (aq) + 4 H_2O = 2 Srp1		
(2a) 3 Cpx + 6 H^+ = Srp1 + 3 Ca^{2+} + 4 SiO_2 (aq) + H_2O		
(2b) 3 Opx + 4 H_2O = 2 Srp1 + 2 SiO_2 (aq)		
(3) 5 Srp1 + 3 Pl + 6 H^+ = 3 Chl1 + 3 Ca^{2+} + 7 SiO_2 (aq) + 2 H_2O		
First stage of rodingitization		
(4) 2 Pl + 5 Cpx + H_2O + 8 H^+ = Hgr + Chl2 + 4 Ca^{2+} + 8.5 SiO_2 (aq)		
(5a) Pl + 2 Ca^{2+} + 0.5 SiO_2 (aq) + 3 H_2O = Hgr + 4 H^+		
(5b) Pl + Ca^{2+} + SiO_2 (aq) + 2 H_2O = Prh +2 H^+		
(5c) Prh + Ca^{2+} + H_2O = Grs + 2 H^+ + 0.5 SiO_2 (aq)		
Second stage of rodingitization		
(6) Hgr + 6 Mg^{2+} + 3.5 SiO_2 (aq) + 9 H_2O = Di + Chl2 + 2 Ca^{2+} + 12 H^+		
Decomposition and carbonation stage		
(7) Grs + 5 Di + 4 H_2O + 8 CO_2 = 8 Cc + Chl2 + 10 SiO_2 (aq)		
Last stage of rodingitization		
(8a) 5 Grs + Di + Chl + 14 Cc + 7 SiO_2 (aq) + 2 H_2O = 3 Ves +14 CO_2		
(8b) 5 Grs + Di + Chl + 14 Ca2+ + 7 SiO_2 (aq) + 16 H_2O = 3 Ves +28 H^+		

Reaction occurring at: (i) GG and MR (black), (ii) prevalently GG and subordinately MR (blue)-, (iii) GG (red), (iv) MR (green).

hypothesis could be confirmed for meteoric-derived fluid, for which talc starts to precipitate when tremolite is back reacted. However, talc appears in activity diagrams only if $\log[SiO_2(aq)] \geq -2$. Second hypothesis coincides with the following activities in the seawater-derived reaction path: $\log[SiO_2(aq)] = -3.2$, $\log[Ca^{2+}/(H^+)^2] = 8.9$, $\log[Mg^{2+}/(H^+)^2] = 6.4$. In both cases, the obtained model did not foresee grossular and prehnite. In particular, prehnite saturation is not reached if vesuvianite, the most volumetrically important phase in the models, is included in the model. Differently, if vesuvianite precipitation is precluded (e.g. for kinetic reasons), grossular starts to precipitate. In this case, reaction path is forced to progress on the grossular-clinochlore field limits (Fig. 10b) up to prehnite saturation (grossular back-reaction in Supplementary Material S3). This coincides with the reverse of reaction 5c. Finally, when vesuvianite is disabled from activity diagram, the field of xonotlite appears (Fig. 10b). This phase was found at GG by Biagioni (2001).

6.3. Element mobilization

Fluids rich in FeO, MnO, MgO, in addition to CaO and SiO_2, have infiltrated the ultramafic rocks of Groppo di Gorro and Mt. Rocchetta (Fig. 9) forming the investigated rodingites. The mass gain of Fe_2O_3 in the rodingites is evidenced by the occurrence of Fe^{3+}-bearing garnet and vesuvianite at GG. According to Beard and Hopkinson (2000), the presence of andradite associated with serpentine and magnetite at MR suggests fO_2 values slightly higher than iron-magnetite (IM) and several log units lower than fayalite-magnetite-quartz (QFM) oxygen buffer. Furthermore, this mineral association requires activities of Ca and Fe and/or the pH of the fluid higher than those of seawater (Beard and Hopkinson, 2000). The oscillatory zoning of Mt. Rocchetta garnet may be due to fluctuation in composition of the hydrothermal fluids, variation in temperature (Jamtveit, 1999) and increasing of oxygen fugacity during the cooling stages of rodingitization (Dubińska et al., 2004).

The studied rodingites show a partial enrichment in Ti, V and in some cases Zr; according to the literature (Dubińska, 1997; Beard and Hopkinson, 2000; Knauss et al., 2001), alkaline fluids rich in Ca and Mg that can be produced during serpentinization favour the mobility of these elements. They can be transported as F^-, Cl^-, PO_4^{2-}, OH^-, SO_4^{2-} and CO_3^{2-} complexes. However, the serpentine and chlorite compositions suggest that the prevailing complexes were OH^-, Cl^- and SO_4^{2-}, besides CO_3^{2-} at Groppo di Gorro, where calcite is present. The mobility of Ti in the solutions is low (Brookins, 1988). However, it can be transported as CO_3^{2-} and OH^- complexes in alkaline solutions (Beard and Hopkinson, 2000; Knauss et al., 2001). The presence of calcite in the rodingite of Groppo di Gorro supports the transport of Ti as CO_3^{2-} complex; the formation of calcite makes the CO_3^{2-} complex unstable. Differently, the lack of calcite at Mt. Rocchetta supports the transport of Ti and Zr as hydroxide complex. In both cases, Ti was partitioned in garnet (TiO_2 up to 26.1 wt.% at GG and 39.5 wt.% at MR).

The samples GG1, GG2, GG3, MR6 have low LREE/HREE ratios (Fig. 8) and show an increase in the mass of REE compared to that of the inferred protoliths (Figs. 8 and 9a, c). This indicates that REEs have been introduced into the system by metasomatic fluids and are hosted in the minerals of the rodingite association. The mobility of REEs is mainly conditioned by the pH value of the solution and by the presence of ligands such as CO_3^{2-}, SO_4^{2-}, OH^- (Mineyev, 1963). In particular, REE are mobilized in medium and high pH fluids and the LREEs form complexes preferably with carbonate ion (Wentlandt and Harrison, 1979; Gimeno Serrano et al., 2000) while the HREEs with hydroxide ion (Haas et al., 1995). In many hydrothermal systems, Al-rich garnet are generally enriched in HREE and depleted in LREE, whereas Fe-rich garnet ($And_{>90}$) contains lower ΣREE with enriched LREE and depleted HREE (Whitney and Olmsted, 1998; Smith et al., 2004; Gaspar et al., 2008). The GG samples have REE patterns (Fig. 8) similar to those of grossular-rich garnet reported in literature for hydrothermal systems (Jamtveit and Hervig, 1994; Gaspar et al., 2008). The MR samples, often containing garnet with oscillatory zoning between andradite and grossular, show REE patterns in some cases similar to those of andradite-bearing rocks (Smith et al., 2004; Gaspar et al., 2008). REE mobilization occurs when the composition of metasomatic fluids is dominant compared to that of the protolith and this occurs when the water/rock ratio is greater than 100 (Tsikouras et al., 2009 and references therein).

6.4. A genetic model

Hydrothermal alteration of the two investigated mantle sequences produced a more or less pervasive serpentinization and crystallization of rodingite assemblages in lherzolites and pyroxenites, both in massive form and veins. The estimated temperatures of the rodingites, based on fluid inclusion microthermometry, are a little higher at Groppo di Gorro (318 °C at 500 bar and 362 °C at 1 kbar) than at Mt. Rocchetta (291 and 334 °C).

The two investigated bodies underwent metasomatism with somewhat different features and intensities depending on the physico-chemical characteristics of the hydrothermal fluids. The petrographic and mineralogical features of Groppo di Gorro rodingites indicate that the hydrothermal alteration and metasomatic processes were pervasive, with complete serpentinization followed by chloritization of the protoliths. In the initial phase of rodingitization, small garnet crystallized at the expense of pyroxene and plagioclase, and calcite precipitated from hydrothermal fluids. Multi-stage infiltration of fluids and prolonged fluid-rock interaction produced an advanced degree of metasomatism culminating with the formation of vesuvianite (second stage of Schandl et al., 1989). Differently, the Mt. Rocchetta mantle body was affected by a smaller extent of rodingite alteration and metasomatism. This is suggested by: (i) the widespread occurrence of primary mineral relics; (ii) the abundance of serpentine, which is only locally transformed into chlorite; (iii) the absence of calcite; (iv) the presence of garnet as the only phase of the rodingite association in some samples; (v) the subordinate amount of diopside with respect to garnet; (vi) the scarcity of vesuvianite.

The hydrothermal processes leading to the formation of the rodingite assemblages may have been related to the late hydration stage associated

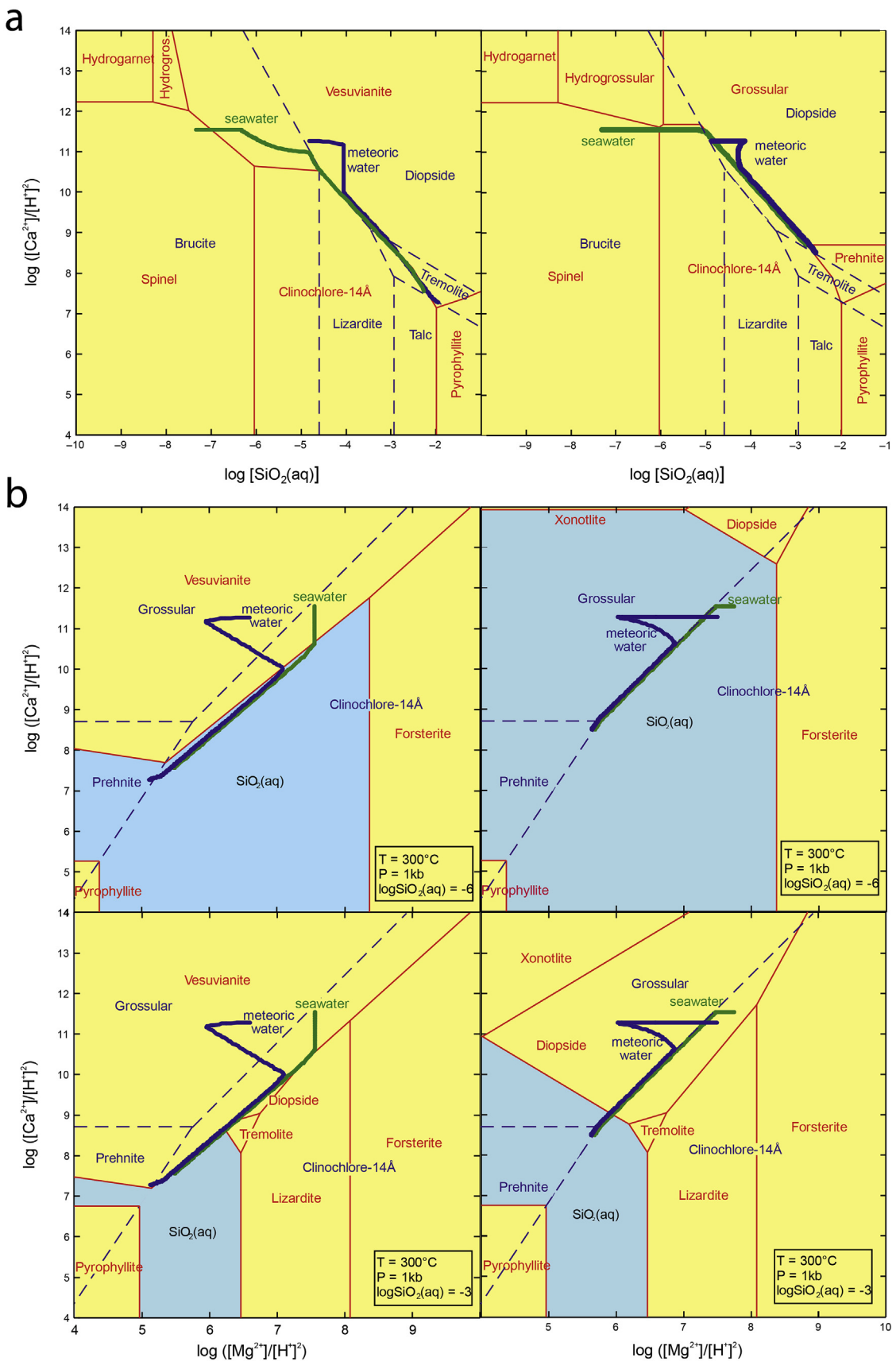

Fig. 10. Activity vs. activity diagrams obtained from the thermodynamic modelling at 300 °C and 1 kbar. In the diagrams with silica activity, the solid red lines show the phase relations of the system CaO–MgO–Al_2O_3–SiO_2–H_2O, whereas the dashed blue lines the phases without Al_2O_3. The green and blue thick lines show the reaction path of the serpentinizing fluids of seawater and meteoric origin, respectively.

with brittle deformation recognized for the External Ligurian mantle sequences (Montanini et al., 2006), i.e. the "F3 stage", when the mantle rocks were exhumed to the seafloor, presumably in Early-Middle Jurassic times. The occurrence of MORB-type gabbroic bodies intruding the Monte Rocchetta sequence suggests that the high-T hydrothermal conditions inferred for this body may have been supported by magmatic activity. Remarkably, thermodynamic modelling has shown that rodingitization is consistent with fluids that have interacted with basaltic flows. Primary contacts between mantle rocks and the volcanic section are lacking in the investigated area, most likely as a consequence of tectonic disruption during the melange formation, but km-sized slide blocks of MOR-type basaltic rocks are widespread in the same ophiolite melange (Casnedi et al., 1993).

Another plausible tectonic setting for the rodingite formation could be the accretionary prism associated with the Late Cretaceous intra-oceanic subduction in the Ligurian Tethys. According to the geological reconstructions, the ophiolitic slide blocks of this study originated from the accretionary prism because of a sedimentary catastrophic event (Malavieille et al., 2016; Marroni et al., 2017 and quoted references). The slide blocks show a low-grade metamorphic history under prehnite-pumpellyite facies conditions ($T \sim 250$ °C) which is broadly consistent with the thermal conditions of the rodingite formation inferred by fluid inclusion study. However, according to our thermodynamic modelling, the precipitation of calcite in the Groppo di Gorro rodingites would require CO_2 fugacity values compatible with the meteoric serpentinizing fluids adopted in the model (see Supplementary Materials S2 and S3). This would imply, in turn, that the Late Cretaceous accretion brought this block of marginal oceanic lithosphere in a continental environment, which is not supported by the geodynamic and geological evidences (Marroni et al., 2017). An alternative explanation to obtain such high CO_2 fugacity may involve interaction between marine fluids and former sedimentary cover of the oceanic lithosphere, i.e. carbonate sediments occurring in the accretionary prism ("Calpionelle" or "Palombini" limestones, Casnedi et al., 1993).

7. Concluding remarks

The ultramafic rocks from Groppo di Gorro and Mt. Rocchetta underwent a complex evolutionary history, which started at high temperature with a mantle decompression and concomitant interaction with melts of asthenospheric origin, producing the crystallization of plagioclase mainly at the expense of Cr-spinel and clinopyroxene. A relatively high-temperature polyphasic metasomatism led to the serpentinization of the primary rocks and subsequent formation of rodingite associations with different features in the two studied mantle bodies.

The average estimated temperatures of rodingitization are relatively high, with slightly higher values at Groppo di Gorro (318 and 362 °C at 500 and 1000 bar, respectively) than at Mt. Rocchetta (291 and 334 °C at 500 and 1000 bar, respectively).

At Groppo di Gorro the alteration was pervasive with complete serpentinization followed by chloritization of the pyroxenite protolith. The association diopside + vesuvianite + garnet (prevalently hydrogrossular) + calcite + chlorite occurred through four stages. (1) formation of hydrogrossular from fluids with high Ca and low silica activities and pH decreasing; (2) appearance of diopside under higher silica activity; (3) formation of chlorite and calcite suggesting infiltration of hydrothermal fluids at mildly oxidizing conditions and high CO_2/H_2O ratio; (4) formation of abundant vesuvianite from H_2O-rich fluids under more reduced conditions.

At Mt Rocchetta the hydrothermal alteration was of lower intensity and the primary minerals of the peridotite and pyroxenite protoliths were partially preserved. The rodingite association consists of garnet + diopside + serpentine ± prehnite ± pumpellyite ± chlorite. Compared to Groppo di Gorro the carbonation stage is absent and the last stage with formation of vesuvianite is very rare. Furthermore, prehnite, diopside and vesuvianite occur only in the former pyroxenite levels. The association of andradite, serpentine and magnetite suggests oxygen fugacity slightly higher than iron-magnetite buffer, Ca and Fe activities and/or the pH of the fluid higher than those of seawater. The oscillatory zoning of Mt. Rocchetta garnet is due to fluctuation in the composition of the hydrothermal fluids owing to oxygen fugacity and temperature variations during the cooling stage.

The hydrothermal processes leading to the formation of the rodingite assemblages may have been related to the late hydration stage associated with (i) the brittle deformation recognized for the External Ligurian mantle sequences or (ii) the accretionary prism formed during the Late Cretaceous intra-oceanic subduction in the Ligurian Tethys.

Declaration of competing interest

The authors declare that they have no known competing financial interests or personal relationships that could have appeared to influence the work reported in this paper.

Acknowledgments

This paper was supported by the University of Parma, Fondi Ricerca Scientifica Locale di Ateneo (Università di Parma) and by MIUR-PRIN prot. 2015C5LN35. This work has also benefited from the equipment and framework of the COMP-HUB Initiative, funded by the 'Departments of Excellence' program of the Italian Ministry for Education, University and Research (Ministero Istruzione Universitá Ricerca, Italy, 2018-856 2022). We thank the Editorial Advisor Prof. Santosh and the Associate Editor Dr. Sohini Ganguly for the assistance and useful suggestions provided. Editorial handling by Lily Wang and constructive reviews and fruitful comments by Marc Ulrich and the anonymous reviewer helped to significantly improve the manuscript and have been greatly appreciated.

Appendix A. Supplementary data

Supplementary data to this article can be found online at https://doi.org/10.1016/j.gsf.2020.04.017.

References

Abbate, E., Bortolotti, V., Principi, G., 1980. Apennine ophiolites: a peculiar oceanic crust. In: Rocci, G. (Ed.), Tethyan Ophiolites, Western Area, vol. 1. Ofioliti Special Issue, pp. 59–96.

Actlabs, 2018. 4Litho - lithium metaborate/tetraborate fusion - ICP and ICP/MS. Webpage: http://www.actlabs.com/page.aspx?page=516&app=226&cat1=549&tp=12&lk=no&menu=64. (Accessed 13 April 2019).

Adorni, F., 2001. Elementi mineralogico-petrografici caratteristici delle ofioliti. La rodingite del Groppo di Gorro (Appennino Parmense). In: Saccani, A. (Ed.), Le Ofioliti: Isole Sulla Terraferma. Atti del Convegno Nazionale, pp. 47–53 (in Italian).

Anders, E., Grevesse, N., 1989. Abundances of the elements: meteoritic and solar. Geochem. Cosmochim. Acta 53, 197–214.

Austrheim, H., Prestvik, T., 2008. Rodingitization and hydration of the oceanic lithosphere as developed in the Leka ophiolite, nort-central Norway. Lithos 104, 177–198.

Auzende, A.L., Daniel, I., Reynard, B., Lemaire, C., Guyot, C., 2004. High-pressure behaviour of serpentine minerals: a Raman spectroscopic study. Phys. Chem. Miner. 31 (5), 269–277.

Bach, W., Klein, F., 2009. The petrology of seafloor rodingites: insights from geochemical reaction path modeling. Lithos 112, 103–117.

Bach, W., Jöns, N., Klein, F., 2013. Metasomatism within the ocean crust. In: Harlov, D.E., Austrheim, H. (Eds.), Metasomatism and the Chemical Transformation of Rock. Springer, Berlin, pp. 253–288.

Bakker, R.J., Brown, P.E., 2003. Computer modelling in fluid inclusion research. In: Samson, I., Anderson, A., Marshall, D. (Eds.), Fluid Inclusions. Analysis and Interpretation. Mineralogical Association of Canada, Short Course Series 32, pp. 175–212.

Barrett, T.J., Spooner, E.T.C., 1977. Ophiolitic breccias associated with allochthonous oceanic crustal rocks in the East Ligurian Apennines, Italy - a comparison with observations from rifted oceanic ridges. Earth Planet Sci. Lett. 35, 79–91.

Barriga, F., Fyfe, W.S., 1983. Development of rodingite in basaltic rocks in serpentinites, East Liguria, Italy. Contrib. Mineral. Petrol. 84, 146–151.

Beard, J.S., Hopkinson, L., 2000. A fossil, serpentinization-related hydrothermal vent, ocean drilling program leg 173, site 1068 (iberia abyssal plain): some aspects of mineral and fluid chemistry. J. Geophys. Res. 15 (B7), 16527–16539.

Beccaluva, L., Macciotta, G., Piccardo, G.B., Zeda, O., 1984. Petrology of lherzolitic rocks from the Northern Apennine ophiolites. Lithos 17, 299–316.
Bersani, D., Andò, S., Vignola, P., Moltifiori, G., Marini, I.-G., Lottici, P.P., Diella, V., 2009. Micro-Raman spectroscopy as a routine tool for garnet analysis. Spectrochim. Acta, Part A 73, 484–491.
Bethke, C.M., Yeakel, S., 2008. The Geochemist's Workbench® - Release 7. GWB Essentials Guide. Hydrogeology Program. University of Illinois, Urbana.
Biagioni, C., 2001. I silicati idrati di calcio: assetto strutturale e comportamento termico. Ph.D. thesis. University of Pisa. https://etd.adm.unipi.it/t/etd-01312011-135501/.
Bill, M., O'Dogherty, L., Guex, J., Baumgartner, P.O., Masson, H., 2001. Radiolarite ages in Alpine-Mediterranean ophiolites: constraints on the oceanic spreading and the Tethys-Atlantic connection. Geol. Soc. Am. Bull. 113, 129–143.
Blanc, P., Lassin, P., Piantone, P., Azaroual, M., Jacquemet, N., Fabbri, A., Gaucher, E.C., 2012. Thermoddem: a geochemical database focused on low temperature water/rock interactions and waste materials. Appl. Geochem. 27, 2107–2116.
Bodnar, R.J., Vityk, M.O., 1994. Interpretation of microthermometric data for H_2O-NaCl fluid inclusions. In: De Vivo, B., Frezzotti, M.L. (Eds.), Fluid Inclusions in Minerals, Methods and Applications. Virginia Tech, Blacksburg, VA, pp. 117–130.
Borghini, G., Rampone, E., Zanetti, A., Class, C., Cipriani, A., Hofmann, A.W., Goldstein, S.L., 2013. Meter-scale Nd isotopic heterogeneity in pyroxenite-bearing Ligurian peridotites encompasses global-scale upper mantle variability. Geology 41, 1055–1058.
Borghini, G., Rampone, E., Zanetti, A., Class, C., Cipriani, A., Hofmann, A.W., Goldstein, S.L., 2016. Pyroxenite layers in Northern Apennines' Upper mantle (Italy) – generation by pyroxenite melting and melt-infiltration reaction. J. Petrol. 57 (4), 625–653.
Borsi, L., Scharer, U., Gaggero, L., Crispini, L., 1996. Age, origin and geodynamic significance of plagiogranites in lherzolites and gabbros of the Piedmont-Ligurian ocean basin. Earth Planet Sci. Lett. 140, 227–241.
Boschetti, T., Etiope, G., Pennisi, M., Romain, M., Toscani, L., 2013b. Boron, lithium and methane isotope composition of hyperalkaline waters (Northern Apennines, Italy): terrestrial serpentinization or mixing with brine? Appl. Geochem. 32, 17–25.
Boschetti, T., Etiope, G., Toscani, L., 2013a. Abiotic methane in the hyperalkaline springs of Genova, Italy. Procedia Earth Planet. Sci. 7, 248–251.
Boschetti, T., Toscani, L., 2008. Springs and streams of the Taro–Ceno Valleys (Northern Apennine, Italy): reaction path modeling of waters interacting with serpentinized ultramafic rocks. Chem. Geol. 257, 76–91.
Boschetti, T., Angulo, B., Cabrera, F., Vásquez, J., Montero, R.L., 2016. Hydrogeochemical characterization of oilfield waters from southeast Maracaibo Basin (Venezuela): diagenetic effects on chemical and isotopic composition. Mar. Petrol. Geol. 73, 228–248.
Brookins, D.G., 1988. Eh-pH Diagrams for Geochemistry. Springer Verlag California, Oregon, and Washington. USGS Bulletin 1247.
Capedri, S., Garuti, G., Rossi, A., 1978. Rodingites from Pindos. Constraint on the "rodingite problem". Neues Jahrbuch Mineral. Abhand. 132, 242–263.
Casnedi, R., Galbiati, B., Vernia, L., Zanzucchi, G., 1993. Note descrittive della carta geologica delle ofioliti del Gruppo di M. Penna e di M.Aiona (Appennino Ligure-Emiliano). Atti Ticinensi Sci. della Terra 36, 231–268 (in Italian).
Coleman, R.G., 1967. Low-temperature Reaction Zones and Alpine Ultramafic Rocks of California. USGS Bulletin, Oregon and Washington, 1247.
Coleman, R.G., 1977. Ophiolites, Ancient Oceanic Lithosphere. Springer, Berlin.
Cortesogno, L., Gaggero, L., Molli, G., 1994. Ocean floor metamorphism in the Piedmont-Ligurian Jurassic basin: a review. Memor. Soc. Geol. Ital. 48, 151–163.
Dal Piaz, G.V., 1969. Filoni rodingitici e zone di reazione a Bassa temperatura al contatto tettonico tra serpentine e rocce incassanti nelle Alpi occidentali italiane. Rendiconti Società Italiana di Mineralogia e Petrologia 25, 263–315 (in Italian).
Dal Piaz, G.V., Di Battistini, G., Gosso, G., Venturelli, G., 1980. Rodingitic gabbro dykes and rodingitic reaction zones in the upper Valtournanche-Breuil area, Piemonte ophiolite nappe, Italian Western Alps. Arch. Sci. Gene. 33, 161–179.
De, A., 1972. Petrology of dikes emplaced in the ultramafic rocks of southeastern Quebec and origin of rodingite. In: Shagam, R., Hargraves, R.B., Morgan, W.J., Van Houten, F.B., Burk, C.A., Holland, H.D., Hollister, L.C. (Eds.), Studies in Earth and Space Sciences, vol. 132. Geological Society of America, pp. 489–501. https://doi.org/10.1130/MEM132-p489.
Deer, W.A., Howie, R.A., Zussman, J., 1992. An Introduction to the Rock-Forming Minerals. Longman Scientific & Technical, Essex, England.
Dilnesa, B.Z., Lothenbach, B., Renaudin, G., Wichser, A., Kulik, D., 2014. Synthesis and characterization of hydrogarnet $Ca_3(Al_x\ Fe_{1-x})_2(SiO_4)_y(OH)_{4(3-y)}$. Cement Concr. Res. 59, 96–111.
Droop, G.T.R., 1987. A general equation for estimating Fe^{3+} concentrations in ferromagnesian silicates and oxides from microprobe analyses using stoichiometric criteria. Mineral. Mag. 51, 431–435.
Dubińska, E., 1995. Rodingites of the eastern part of jordanów–gogołów serpentinite massif, lower silesia, Poland. Can. Mineral. 33, 585–608.
Dubińska, E., 1997. Rodingites and amphibolites from the serpentinites surrounding Sowie Göry block (Lower Silesia, Poland): record of supra-subduction zone magmatism and serpentinization. Neues Jahrbuch Mineral. Abhand. 171, 239–279.
Dubińska, E., Bylina, P., Kozlowski, A., 2004. Garnet from Lower Silesia rodingites: constraints from their chemistry. Pol. Tow. Mineral. Pr. Spec. 24, 135–139.
Elter, P., Marroni, M., Molli, G., Pandolfi, L., 1991. Le caratteristiche stratigrafiche del Complesso di M.Penna/Casanova. Atti Ticinesi di Scienze della Terra 34, 97–106 (in Italian).
Ferrando, S., Frezzotti, M.L., Orione, P., Conte, R.C., Compagnoni, R., 2010. Late-Alpine rodingitization in the Bellecombe meta-ophiolites (Aosta Valley, Italian Western Alps): evidence from mineral assemblages and serpentinization-derived H_2-bearing brine. Int. Geol. Rev. 52, 1220–1243.
Frost, B.R., Beard, J.S., McCaig, A., Condliffe, E., 2008. The formation of micro-rodingites from IODP Hole U1309D: key to understanding the process of serpentinization. J. Petrol. 49, 1579–1588.
Galuskin, E.V., Armbruster, T., Malsy, A., Galuskina, I.O., Sitarz, M., 2003. Morphology, composition and structure of low-temperature P4/nnc high-fluorine vesuvianite whiskers from Polar Yakutia, Russia. Can. Mineral. 41, 843–856.
Gaspar, M., Knaack, C., Meinert, L.D., Moretti, R., 2008. REE in skarn systems: a LA-ICP-MS study of garnets from the Crown Jewel gold deposit. Geochem. Cosmochim. Acta 72, 185–205.
Gimeno Serrano, M.J., Auqué Sanz, L.F., Nordstrom, D.K., 2000. REE speciation in low-temperature acidic waters and the competitive effects of aluminium. Chem. Geol. 165, 167–180.
Grant, J.A., 1986. The isocon diagram: a simple solution of gresens' equation for metasomatic alteration. Econ. Geol. 81, 1976–1982.
Groppo, C., Rinaudo, C., Cairo, S., Gastaldi, D., Compagnoni, R., 2006. Micro-Raman spectroscopy for a quick and reliable identification of serpentine minerals from ultramafics. Eur. J. Mineral 18, 319–329.
Haas, J.R., Shock, E.L., Sassani, D.C., 1995. Rare earth elements in hydrothermal systems: estimates of standard partial molal thermodynamic properties of aqueous complexes of the rare earth elements at high pressures and temperatures. Geochem. Cosmochim. Acta 59, 4329–4350.
Hall, A., Ahmed, Z., 1984. Rare earth content and origin of rodingites. Chem. Erde 43, 45–56.
Hatzipanagiotou, K., Tsikouras, B., 2001. Rodingite formation from diorite in the Samothraki ophiolite, NE Aegean, Greece. Geol. J. 36, 93–109.
Hatzipanagiotou, K., Tsikouras, B., Migiros, G., Gartzos, E., Serelis, K., 2003. Origin of rodingites in ultramafic rocks from lesvos island (NE aegean, Greece). Ofioliti 28, 13–23.
Hawthorne, F.C., Oberti, R., Harlow, G.E., Maresch, W.V., Martin, R.F., Schumacher, J.C., Welch, M.D., 2012. Nomenclature of the amphibole supergroup. Am. Mineral. 97, 2031–2048.
Hey, M.H., 1954. A new review on the chlorite. Mineral. Mag. 224, 277–298.
Holland, T.J.B., Powell, R., 2011. An improved and extended internally consistent thermodynamic dataset for phases of petrological interest, involving a new equation of state for solids. J. Metamorph. Geol. 29, 333–383.
Honnorez, J., Kirst, P., 1975. Petrology of rodingites from the equatorial Mid-Atlantic fracture zones and their geotectonic significance. Contrib. Mineral. Petrol. 49, 233–257.
Jamtveit, B., 1999. Crystal growth and intracrystalline zonation patterns in hydrothermal environments. In: Jamtveit, B., Meakin, P. (Eds.), Growth, Dissolution and Pattern Formation in Geosystems. Kluwer Academic Publishers, Dordrecht, pp. 65–84.
Jamtveit, B., Hervig, R.L., 1994. Constraints on transport and kinetics in hydrothermal systems from zoned garnet crystals. Science 263 (5146), 505–508.
Keighley, D., 2013. Outcrop Chemostratigraphic Correlation of the Upper Green River Formation in the Uinta Basin, Utah - Mahogany Oil Shale Zone to the Uinta Formation. Miscellaneous Publication 13-1. Utah Geological Survey, a division of Utah Department of Natural Resources. http://digitallibrary.utah.gov/awweb/guest.jsp?smd=1&cl=all_lib&lb_document_id=63453.
Kleppe, A.K., Jephcoat, A.P., Welch, M.D., 2003. The effect of pressure upon hydrogen bonding in chlorite: a Raman spectroscopy study of clinochlore to 26.5 GPa. Am. Mineral. 88, 567–573.
Knauss, K.G., Dibley, M.J., Bourcier, W.L., Shaw, H.F., 2001. Ti(IV) hydrolysis constants derived from rutile solubility measurements made from 100 to 300°C. Appl. Geochem. 16, 1115–1128.
Knight, C.L., Bodnar, R.J., 1989. Synthetic fluid inclusions. IX. Critical PVTX properties of NaCl-H_2O solutions. Geochem. Cosmochim. Acta 53, 3–8.
Kolesov, B.A., Geiger, C.A., 2005. The vibrational spectrum of synthetic hydrogrossular (katoite) $Ca_3Al_2(O_4H_4)_3$: a low-temperature IR and Raman spectroscopic study. Am. Mineral. 90, 1335–1341.
Kong, X.K., Tutolo, B.M., Saar, M.O., 2013. DBCreate: a SUPCRT92-based program for producing EQ3/6, TOUGHREACT and GWB thermodynamic databases at user defined T and P. Comput. Geosci. 51, 415–417.
Koutsovitis, P., Magganas, A., Pomonis, P., Ntaflos, T., 2013. Subduction-related rodingites from East Ophris, Greece: mineral reactions and physicochemical conditions of formation. Lithos 172–173, 139–157.
Koutsovitis, P., Magganas, A., Ntaflos, T., Koukouzas, N., 2018. Rodingitization and carbonation, associated with the serpentinization of Triassic ultramafic cumulates and lavas in Othris, Greece. Lithos 320–321, 35–48.
Lemaire, C., Guyot, F., Reynard, B., 1999. Vibrational Spectroscopy (IR and Raman) of OH Group in Chrysotile Lizardite and Antigorite, vol. 10. European Union of Geosciences, Strasbourg, p. 654.
Li, X.P., Rahn, M., Bucher, K., 2004. Metamorphic processes in rodingites of the Zermatt-Saas ophiolites. Int. Geol. Rev. 46, 28–51.
Li, X.P., Zhang, L., Wei, C., Ai, Y., Chen, J., 2007. Petrology of rodingite derived from eclogite in western Tianshan, China. J. Metamorph. Geol. 25, 363–382.
Malavieille, J., Molli, G., Genti, M., Dominguez, S., Beyssac, O., Taboada, A., Chen, C.T., 2016. Formation of ophiolite-bearing tectonosedimentary mélanges in accretionary wedges by gravity driven submarine erosion: insights from analog models and case studies. J. Geodyn. 100, 87–103.
Marini, L., Ottonello, G., 2002. Atlante degli acquiferi della Liguria. Volume III: Le acque dei complessi ofiolitici (bacini: Arrestra, Branega, Cassinelle, Cerusa, Erro, Gorzente, Leira, Lemme, Lerone, Orba, Piota, Polcevera, Rumaro, Sansobbia, Stura, Teiro, Varenna, Visone). Pacini, Pisa (in Italian).
Marroni, M., Treves, B., 1998. Hidden terranes in the northern Apennines, Italy: a record of late cretaceous – oligocene transpressional tectonics. J. Geol. 106, 149–164.

Marroni, M., Meneghini, F., Pandolfi, L., 2017. A revised subduction inception model to explain the late cretaceous, double-vergent orogen in the precollisional western Tethys: evidence from the northern Apennines. Tectonics 36, 2227–2249.
Marroni, M., Molli, G., Ottria, G., Pandolfi, L., 2001. Tectono-sedimentary evolution of the External Liguride units (Northern Apennine, Italy): insight in the precollisional history of a fossil ocean-continent transition zone. Geodin. Acta 14, 307–320.
Matschei, T., Lothenbach, B., Glasser, F.P., 2007. Thermodynamic properties of portland cement hydrates in the system $CaO–Al_2O_3–SiO_2–CaSO_4–CaCO_3–H_2O$. Cement Concr. Res. 37, 1379–1410.
McCollom, T.M., Shock, E.L., 1997. Geochemical constraints on chemolithoautotrophic metabolism by microorganisms in seafloor hydrothermal systems. Geochem. Cosmochim. Acta 61, 4375–4391.
Mineyev, D.A., 1963. Geochemical differentiation of the rare earths. Geokhimiya 12, 1082–1100.
Mittwede, S.K., Schandl, E.S., 1992. Rodingites from the southern appalchian piedmont, South Carolina, USA. Eur. J. Mineral 4, 7–16.
Molli, G., 1996. Pre-orogenic tectonic framework of the northern Apennine ophiolites. Eclogae Geol. Helv. 89, 163–180.
Montanini, A., Tribuzio, R., 2015. Evolution of recycled crust within the mantle: constraints from the garnet pyroxenites of the External Ligurian ophiolites. N Apennine, Italy. Geology 43, 911–914.
Montanini, A., Tribuzio, R., Anczkiewicz, R., 2006. Exhumation history of a garnet pyroxenite-bearing mantle section from a continent-ocean transition (Northern Apennine ophiolites, Italy). J. Petrol. 47, 1943–1971.
Montanini, A., Tribuzio, R., Thirlwall, M., 2012. Garnet clinopyroxenite layers from the mantle sequences of the Northern Apennine ophiolites (Italy): evidence for recycling of crustal material. Earth Planet Sci. Lett. 351–352, 171–181.
Montanini, A., Tribuzio, R., Van Acken, D., 2017. Multiple events of melt-rock interaction recorded by undeformed spinel pyroxenites from the External Ligurian ophiolites. In: Congresso SIMP-SGI-SOGEI-AIV, Pisa Geosciences: a Tool in a Changing World.
Montanini, A., Tribuzio, R., Vernia, L., 2008. Petrogenesis of basalts and gabbros from an ancient continent-ocean transition (External Liguride ophiolites, Northern Italy). Lithos 101, 453–479.
Morse, S.A., 1980. Basalts and Phase Diagrams: an Introduction to the Quantitative Use of Phase Diagrams in Igneous Petrology. Springer-Verlag, New York.
Müntener, O., Piccardo, G.B., 2003. Melt migration in ophiolitic peridotites: the message from Alpine-Appennine peridotites and implications for embryonic ocean basins. In: Dilek, Y., Robinson, P.T. (Eds.), Ophiolites in Earth History, vol. 218. Geological Society of London, Special Publications, pp. 1–21.
Naylor, M., 1982. The Casanova Complex of northern Apennines: a melange formed on a distal passive continental margin. J. Struct. Geol. 4, 1–18.
O'Hanley, D.S., 1996. Serpentinites: Records of Tectonic and Petrological History. Oxford University Press, New York, p. 277.
O'Hanley, D.S., Schandl, E.S., Wicks, F.J., 1992. The origin of rodingites from Cassiar, British Columbia, and their use to estimate T and $P(H_2O)$ during serpentinization. Geochem. Cosmochim. Acta 56, 97–108.
Palandri, J.L., Reed, M.H., 2004. Geochemical models of metasomatism in ultramafic systems: serpentinization, rodingitization, and sea floor carbonate chimney precipitation. Geochem. Cosmochim. Acta 68, 1115–1133.
Petriglieri, J.R., 2017. Alteration of asbestiform minerals under sub-tropical climate: mineralogical monitoring and geochemistry. Ph. D. thesis. In: The Example of New Caledonia. University of New Caledonia and University of Parma.
Petriglieri, J.R., Salvioli-Mariani, E., Mantovani, L., Tribaudino, M., Lottici, P.P., Laporte-Magoni, C., Bersani, D., 2015a. Micro-Raman mapping of the polymorphs of serpentine. J. Raman Spectrosc. 46, 953–958.
Petriglieri, J.R., Salvioli-Mariani, E., Costa, S., Mantovani, L., Tribaudino, M., D'Alessio, D., Bersani, D., Lottici, P.P., 2015b. Preliminary study on plymorphs of serpentine present in the ophiolites from La Rocchetta (Taro valley, eastern ligurian Apennines, Italy) Congresso SIMP Rendiconti Online Società Geologica Italiana 35 (2), 52.
Piccardo, G.B., Müntener, O., Zanetti, A., 2004. Alpine-Apennine ophiolitic peridotites: new concepts on their composition and evolution. Ofioliti 29, 63–74.
Pomonis, P., Tsikouras, B., Karipi, S., Hatzipanagiotou, K., 2008. Rodingite formation in ultramafic rocks from the Kozikas ophiolite, Western Thessaly, Greece: conditions of metasomatic alteration, geochemical exchanges and $T\text{-}X(CO_2)$ evolutionary path. Can. Mineral. 46, 569–581.
Prieto, A.C., Dubessy, J., Cathelineau, M., 1991. Structure composition relationships in trioctahedral chlorites: a vibrational spectroscopy study. Clay Clay Miner. 39, 531–539.
Rampone, E., Hofmann, A.W., Piccardo, G.B., Vannucci, R., Bottazzi, P., Ottolini, L., 1995. Petrology, mineral and isotope geochemistry of the external liguride peridotites (northern appennine, Italy). J. Petrol. 36, 81–105.
Rickwood, P.C., 1968. On recasting analyses of garnet into end-member molecules. Contrib. Mineral. Petrol. 18, 175–198.
Rice, J.M., 1983. Metamophism of rodingites: part I, Phase relations in a portion of the system $CaO\text{-}MgO\text{-}Al_2O_3\text{-}SiO_2\text{-}CO_2\text{-}H_2O$. Am. J. Sci. 283-A, 121–150.
Rösli, U., Hoernes, S., Köppel, V., 1991. Isotope data of metarodingites and associated rocks from the Lanzo and the Bracco ophiolitic massifs: indications on the evolution of the Alpino-type ultramafic-mafic complexes. Schweiz. Mineral. Petrogr. Mittl. 71, 125–141.
Sanfilippo, A., Tribuzio, R., 2011. Melt transport and deformation history in a "non-volcanic" ophiolitic section (Northern Apennine, Italy): implications for crustal accretion at slow spreading settings. G-cubed 12, 1–34.
Schandl, E.S., Mittwede, S.K., 2001. Evolution of acipayam (denizli, Turkey) rodingites. Int. Geol. Rev. 43, 611–623.
Schandl, E.S., O'Hanley, D.S., Wicks, F.J., 1989. Rodingites in serpentinized ultramafic rocks of the Abitibi greenstone belt, Ontario. Can. Mineral. 57, 579–591.
Schandl, E.S., O'Hanley, D.S., Wicks, F.J., Kyser, K., 1990. Fluid inclusion in rodingite: a geothermometer for serpentinizazion. Econ. Geol. 85, 1273–1276.
Schwartz, S., Guillot, S., Reynard, B., Lafay, R., Debret, B., Nicollet, C., Lanari, P., Auzende, A.L., 2013. Pressure-temperature estimates of the lizardite/antigorite transition in high pressure serpentinites. Lithos 178, 197–210.
Smith, M.P., Henderson, P., Jeffries, T.E.R., Long, J., Williams, C.T., 2004. The rare earth elements and uranium in garnets from the beinn an dubhaich aureole, skye, scotland, UK: constraints on processes in a dynamic hydrothermal system. J. Petrol. 45, 457–484.
Sparkes, G.W., 2017. Geochemical Data from the Central Mineral Belt of Labrador. Open File LAB/1692, Newfoundland Labrador Natural Resources - Mines. March, 2017, p. 209. St. John's, Newfoundland, Canada. https://www.nr.gov.nl.ca/nr/mines/geoscience/publications/openfiles/OF_LAB_1692/OF_LAB_1692.pdf.
Sun, S.S., 1982. Chemical composition and origin of the earth's primitive mantle. Geochem. Cosmochim. Acta 46, 179–192.
Tagirov, B., Schott, J., 2001. Aluminum speciation in crustal fluids revisited. Geochem. Cosmochim. Acta 65, 3965–3992.
Tribuzio, R., Thirwall, M.F., Vannucci, R., 2004. Origin of the gabbro–peridotite association from the Northern Apennine ophiolites (Italy). J. Petrol. 45, 1109–1124.
Tribuzio, R., Renna, M.R., Dallai, L., Zanetti, A., 2014. The magmatic–hydrothermal transition in the lower oceanic crust: clues from the Ligurian ophiolites, Italy. Geochem. Cosmochim. Acta 130, 188–211.
Tribuzio, R., Garzetti, F., Corfu, F., Tiepolo, M., Renna, M.R., 2016. U–Pb zircon geochronology of the Ligurian ophiolites (Northern Apennine, Italy): implications for continental breakup to slow seafloor spreading. Tectonophysics 666, 220–243.
Tsikouras, B., Karipi, S., Hatzipanagiotou, K., 2013. Evolution of rodingites along stratigraphic depth in the Iti and Kallidromon ophiolites (central Greece). Lithos 175–176, 16–29.
Tsikouras, B., Karipi, S., Rigopoulos, I., Perraki, M., Pomonis, P., Hatzipanagiotou, K., 2009. Geochemical processes and petrogenetic evolution of rodingite dykes in the ophiolite complex of Othrys (Central Greece). Lithos 113, 540–554.
Venturelli, G., Contini, S., Bonazzi, A., Mangia, A., 1997. Weathering of ultramafic rocks and element mobility at Mt. Prinzera, Northern Apennines, Italy. Mineral. Mag. 61, 765–778.
Vescovi, P., Andreozzi, M., De Nardo, M.T., Lasagna, S., Martelli, L., Rio, D., Tellini, C., Vernia, L., 2002. Note illustrative della carta geologica d'Italia alla scala 1:50.000, F.° 216, "Borgo Val di Taro" Regione Emilia Romagna, S.El.CA Firenze Ed, pp. 1–115 (in Italian).
Wang, A., Freeman, J.J., Jolliff, B.L., 2015. Understanding the Raman spectral features of phyllosilicates. J. Raman Spectrosc. 46, 829–845.
Wentlandt, R.F., Harrison, W.J., 1979. Rare earth partitioning between immiscible carbonate and silicate liquids and CO_2 vapor: results and implications for the formation of light rare earth-enriched rocks. Contrib. Mineral. Petrol. 69, 409–419.
Whitney, P.R., Olmsted, J.F., 1998. Rare earth element metasomatism in hydrothermal systems: the Willsboro-Lewis wollastonite ores, New York, USA. Geochem. Cosmochim. Acta 62, 2965–2977.
Wilson, J.C., 2010. A new polymer model for estimating Gibbs free energy of formation (ΔGf) of 7, 10 and 14 Å phyllosilicates at 25 °C, 1 Bar. In: Clays in Natural and Engineered Barriers for Radioactive Waste Confinement: 4th International Meeting, March 2010, Nantes, France, p. 475.
Wolery, T.W., Jarek, R.L., 2003. EQ3/6, Version 8.0 - Software User's Manual. Civilian Radioactive Waste, Management System, Management & Operating Contractor. Sandia National Laboratories, Albuquerque, New Mexico. http://www.wipp.energy.gov/%5C/library/CRA/CRA-2014/References/Others/Wolery_Jarek_2003_Software_Users_Manual_EQ36_Version_8_0.pdf.
Wolery, T.W., Jove-Colon, C., 2007. Qualification of Thermodynamic Data for Geochemical Modeling of MineraleWater Interactions in Dilute Systems. Sandia National Laboratories. https://www.nrc.gov/docs/ML0907/ML090770163.pd.
Zhang, Y.G., Frantz, J.D., 1987. Determination of the homogenization temperatures and densities of supercritical fluids in the system $NaCl–KCl–CaCl_2–H_2O$ using synthetic fluid inclusions. Chem. Geol. 64, 335–350.